

Conceptual Design of Highly-Constrained Splitters for the FFA@CEBAF Energy Upgrade Study

R.M. Bodenstein^{a,*}, J.F. Benesch^a, A.M. Coxe^b, K.E. Deitrick^a,
B. Freeman^a, B.R. Gamage^a, R. Kazimi^a, D.Z. Khan^a, K.E. Price^a,
B. Schaumloffel^a

^a*Thomas Jefferson National Accelerator Facility, Newport News, VA, USA*

^b*Virginia Commonwealth University, Richmond, VA, USA*

Abstract

The Continuous Electron Beam Accelerator Facility (CEBAF) at Jefferson Lab is investigating a significant energy upgrade utilizing Fixed-Field Alternating-gradient (FFA) recirculating arcs. This upgrade requires the design of complex horizontal beam splitters to manage up to six concurrent beam passes. This paper presents the conceptual design of these splitters, which are subject to severe physical constraints imposed by the existing accelerator tunnel and multifaceted beam dynamics requirements for matching into the permanent-magnet FFA arcs. The design methodology, centered on multi-pass simulations in the Bmad toolkit, is detailed from the initial geometric layout through the advanced optics matching. Key results include a robust geometric arrangement that fits within the spatial boundaries and the development of multiple, flexible optics matching solutions. Furthermore, the design integrates a viable scheme for extracting high-energy beams for the experimental halls, a critical operational requirement. This work establishes a comprehensive and viable conceptual design, forming a baseline for future engineering and performance optimization studies.

Keywords: CEBAF, Beam Splitter, Accelerator Upgrade, Accelerator Design, Beam Dynamics, Lattice Design, FFA, Fixed-Field Alternating Gradient, Beam Optics

*Corresponding Author

Email address: ryanmb@jlab.org (R.M. Bodenstein)

1. Introduction

This section will briefly describe the Continuous Electron Beam Accelerator Facility (CEBAF) to remind the readers of the current machine, as well as its possible future. Relevant background information will be provided, as well as a description of the FFA@CEBAF energy upgrade study.

1.1. CEBAF Background

The Continuous Electron Beam Accelerator Facility (CEBAF) is a recirculating linear accelerator (RLA) capable of accelerating polarized electrons up to a nominal maximum energy of 12 GeV. CEBAF consists of two superconducting LINACs, each capable of reaching 1090 MeV. Each LINAC is connected by a stack of recirculating arcs, which magnetically spread the beam into energy-separated beamlines, bends the separated beams 180° , and recombines them to be launched into the next LINAC.

In order to separate the different energy passes, each recirculating arc starts with a beam separation system, referred to locally (and throughout this paper) as the spreader. The spreader bends the beams in an upward trajectory using common dipoles, sending the lowest-energy beams furthest up due to the beam's lowest rigidity. Each successive pass is bent upward to a lesser degree. Each pass is then further separated through a two-step elevation change. These two steps are used in conjunction with three quadrupoles to control the dispersion and the optics, so that upon entering the arc proper, the optics are achromatic. After matching and transporting, the different passes are recombined in a section called the recombiner, which is designed to be a mirror image of the spreader. The beams are recombined and matched into the LINAC. There are five recirculating arc beamlines on each of the east and west sides of CEBAF, while the LINACs occupy the north and south areas.

CEBAF has four experimental halls: three on the southwest corner named Halls A, B, and C, and one on the northeast corner, named Hall D. To extract the beam to Halls A, B, and C, an RF separator system is used, which provides transverse kicks to the beam at the desired energy for the experiment. This RF kicker system takes advantage of CEBAF's fundamental frequency of 1497 MHz, and the timing of the bunch structure for the beams assigned to each experimental hall. As beams pass through the RF kicker system, they are either kicked out toward the extraction system toward Halls A, B, and C, or allowed further recirculations to gain more energy.

Hall D is only capable of taking the top operating energy. Located in the northeast corner of the lab, it was added during the 12 GeV Upgrade. Instead of an RF kicker system in the northeast corner, a 750 MHz Separator is used in the southwest corner to allow Hall D beams to pass through the West Arc and North LINAC one additional time, sending ~ 12 GeV beam to the Hall.

1.2. The FFA@CEBAF Energy Upgrade

CEBAF has roughly a decade of planned physics experiments that have been approved and scheduled to occur. After these experiments are completed, the future of CEBAF is uncertain. Furthermore, with the current plans for the Electron Ion Collider (EIC) to be constructed at Brookhaven National Lab (BNL), any future plans for studies at CEBAF should not overlap with the studies that can be performed at EIC. However, the parameter space is broad enough that interesting physics still exists, both by ways of complimentary studies and new, refined studies.

Jefferson Lab is currently looking at two possible upgrades to CEBAF that will allow such studies. It has been proposed that, at the end of the planned physics schedule, CEBAF undergoes an upgrade to allow for positron studies. For more information on this upgrade, please see [1, 2].

After the positron experiments are completed, another upgrade proposal is to increase the energy reach of CEBAF. To accomplish this, rather than major upgrades to the LINACs, a smaller-scale proposal has been put forward: using Fixed-Field Alternating gradient (FFA) recirculating arcs (similar in concept to those of the Cornell BNL ERL Test Accelerator (CBETA)) to increase the total number of passes through the pair of LINACs, thus increasing the total achievable energy. In short, the current highest-energy recirculating arcs in both the east and west sides of CEBAF would be replaced with multipass FFA arcs, each allowing five or six passes, thus adding four or five additional passes through the LINACs, increasing the total achievable energy. This FFA@CEBAF study aims for an energy of over 20 GeV, with numbers such as 22 GeV being discussed as a possible future goal [3]. The feasibility of this upgrade is being studied, and the details are discussed [3, 4]. The total final energy, as well as the science case, is yet to be fully determined.

The FFA arcs will utilize Halbach-style permanent magnet arrays, which offer a compact solution for multipass acceleration [5, 6]. While these magnets will include small Panofsky-style multipole correctors for fine-tuning [7–

11], they are otherwise non-adjustable. This fixed-field nature necessitates precise control of the beam parameters at the entrance to the FFA arcs to ensure stable transport for all six passes.

1.3. The Need for a Horizontal Splitter

To achieve the required precision, dedicated beamlines known as horizontal splitters are essential. Drawing on experience from the CBETA facility [12], these splitters are designed to receive the co-linear bunch of up to six FFA-bound passes from the main linac and separate them horizontally into six independent beamlines. Within these lines, the optics for each pass must be individually manipulated to meet the strict matching conditions of the FFA arc.

This independent control must address multiple parameters simultaneously: the Twiss parameters (α, β) , dispersion and its derivative (η, η') , time-of-flight (ToF), and the momentum compaction term (R_{56}). Unlike the existing CEBAF arcs, the FFA arcs will not contain dogleg chicanes for path-length correction, shifting this crucial function entirely to the upstream splitters.

1.4. Design Philosophy and Approach

The design process was guided by a conservative philosophy best summarized as, “measure twice, cut once.” A pessimistic view was maintained, incorporating as many realistic constraints and design restrictions as possible from the outset, as it is far simpler to relax constraints later than to add them to a mature design. The primary focus was on achieving operational robustness, simplicity, and flexibility.

To this end, the conceptual design relies exclusively on conventional linear electromagnets that are either already in use at CEBAF, or are based on detailed designs produced for this project [13–22]. The dipoles were modeled with deliberately large transverse dimensions (0.5 m width in X and Y planes) to ensure ample flexibility for future magnet engineering and to guarantee that the layout could accommodate realistic components. The quadrupoles selected for use are already in use in the current CEBAF machine. The limits placed on the optimization routine were conservative, both to allow for them to be scaled in strength for the higher-energy southwest splitters, and to maintain magnet strength overhead in the worst-case scenarios.

While multifunction magnets present a potential alternative, they were excluded due to both the nonlinearities that real multifunction magnets introduce, and because they add a level of complexity which should only be used when needed. Since CEBAF does not currently use any nonlinear magnets, introducing nonlinear terms will complicate the overall operation of the accelerator.

1.5. Scope of this Paper

This paper presents the comprehensive conceptual design of the horizontal splitter for the FFA@CEBAF upgrade. Section 2 details the severe physical, geometrical, and beam dynamics constraints that define the design challenge. Section 3 describes the development of the geometric layout, including the magnet choices and the multi-pass separation and recombination scheme. Section 4 presents the results of the optics design and matching simulations, demonstrating multiple viable solutions. Section 5 outlines the proposed scheme for high-energy beam extraction. Finally, Section 6 summarizes the current status and discusses the direction of future work.

2. Design Constraints and Requirements

2.1. Physical and Geometrical Constraints

As an upgrade, the splitter must be installed within the existing CEBAF tunnel, leading to highly restrictive spatial constraints. The design must preserve a mandated personnel access aisle (1.118 m) and accommodate existing tunnel infrastructure. The available space was determined from detailed measurements of the tunnel in the relevant regions. The primary transverse and longitudinal constraints, assuming the splitter occupies the spreader and extraction regions, are summarized in Table 1.

Table 1: Summary of the primary physical constraints placed upon the splitter design geometry, derived from engineering measurements of the CEBAF tunnel [23].

Name	Plane	Value	Units
Wall to Beamline Center	Horizontal	1.3716	m
Beamline Center to Personnel Clearance Limit	Horizontal	1.5665	m
Total Available Transverse Space	Horizontal	2.939	m
LINAC Beam Height in CEBAF Coordinates	Vertical	y=100	m
Total Length in Z (to End of Final Magnet)	Longitudinal	z=92	m

An important note is that only the northeast and southwest corners of the CEBAF machine have adequate longitudinal space to accommodate these splitters, as the LINACs start near the beginning of each straight section, but end well before the end of the straight section. Furthermore, there are only two access points into the CEBAF tunnel with crane access for heavy equipment. They are located in the northwest and southeast corners. This limits the ability to place two splitters on each recirculating arc like CBETA, and instead requires one splitter at the beginning of each arc. This also increases the burden on each single splitter.

A graphical representation of the transverse space is shown in Figure 1, illustrating the asymmetric transverse space available relative to the nominal beamline center.

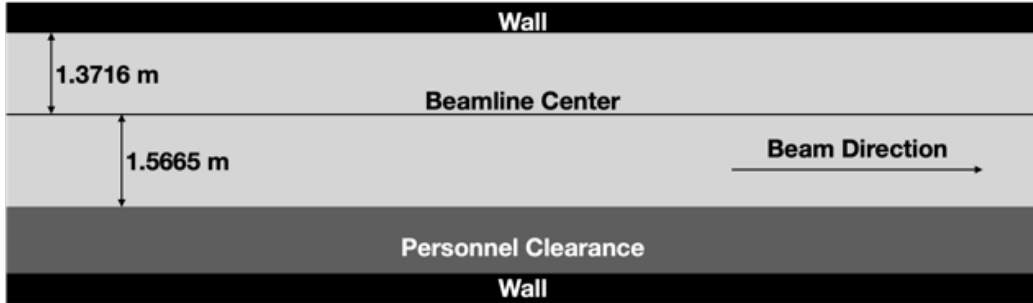


Figure 1: Diagram of the transverse constraints in the CEBAF tunnel.

2.2. Beam Dynamics Requirements

Each of the six passes enters the FFA arc at a unique energy and must be delivered to a specific, non-collinear horizontal position with precisely matched optics. The required input parameters for each pass at the entrance of the east FFA arc is listed in Table 2. Please note, these parameters are match points at the beginning of an FFA cell, but the design of the FFA arcs are likely to change, necessitating changes in the matching parameters. Furthermore, different match points within the FFA cell can be used, as each cell is made up of segments, and the starting point can be adjusted as needed. This will be described further later in the paper.

It is also important to note the spread of X values listed in Table 2. There is a ~ 3 cm difference between the highest and lowest energy passes. This value changes depending upon the match point within an FFA cell, and

version of the FFA arc optics as well. They are also all negative values due to coordinate system definitions.

Table 2: Example entrance match parameters for the east FFA Arc. These values are at the entrance to the FFA Arc. Other match points in the FFA Cell can be used: this will be described later.

Pass (E)	X (m)	Px	β_x (m)	α_x	β_y (m)	α_y	η (m)	η'
1 (10.55 GeV)	-4.3609E-02	1.5555E-02	4.1508	3.0414	6.5160	-3.1904	1.3845E-02	-2.7713E-03
2 (12.95 GeV)	-4.0953E-02	1.4756E-02	2.9513	1.8208	6.4812	-3.0391	3.4001E-02	-1.1549E-02
3 (14.95 GeV)	-3.6297E-02	1.3082E-02	2.7191	1.5387	7.0035	-3.2108	5.0554E-02	-1.8809E-02
4 (17.15 GeV)	-2.9986E-02	1.0682E-02	2.6034	1.3996	8.0521	-3.6443	6.4348E-02	-2.4885E-02
5 (19.35 GeV)	-2.2289E-02	7.6691E-03	2.5224	1.3113	10.173	-4.5685	7.5975E-02	-3.0021E-02
6 (21.55 GeV)	-1.3418E-02	4.1373E-03	2.4564	1.2473	17.058	-7.6233	8.5873E-02	-3.4401E-02

On top of optics matching requirements, the splitters must manage the ToF and R_{56} for each pass. The ToF must be controlled to within a fraction of an RF degree to ensure proper acceleration in the subsequent linac pass. This requires compensating for the path length differences between the passes within the FFA arcs and also adjusting for thermal expansion and contraction of the accelerator throughout the year, a variation that currently requires daily adjustment of CEBAF's dogleg magnets.

2.3. Operational Requirements

Beyond the primary beam dynamics functions, the splitter design must incorporate several key operational features. First, it must provide a mechanism for extracting the high-energy FFA passes to the experimental halls, as no other system is planned for this purpose. Second, the layout must reserve adequate space for essential beamline hardware, including beam position monitors (BPMs), diagnostic viewers, corrector magnets, vacuum pumps, and valves, without which the system cannot be reliably commissioned or operated.

3. Geometric Layout

The geometric design process prioritized fitting all necessary components into the constrained space before optimizing the optics. The Bmad simulation toolkit [24] was used for this task due to its ability to model multiple beamlines with realistic, solid magnet geometries simultaneously.

3.1. Magnet and Component Design

The design utilizes two main types of dipoles: 3 m long main dipoles and a few shorter 1.5 m dipoles for smaller chicanes. All are modeled as 0.5 m wide electromagnets, based on conservative engineering analysis which established a field limit of approximately 1.8 T [21]. These designs are specifically made thick as a further design constraint: if the geometry works with magnets of this size but the tolerances are too tight, it is possible to make these dipoles thinner in the relevant plane. Using oversized models for the dipoles ensures that any future, more optimized magnet designs will fit within the established layout. The quadrupoles used in this design are already existing CEBAF QR-type magnets [25], which are well-understood and capable of providing the required gradients. Care was taken to limit the quadrupole strengths in the simulations so that they can be scaled for the higher-energy southwest splitters and still maintain adequate overhead for the quadrupoles.

3.2. Multi-Pass Separation Scheme

The six beam passes enter the splitter co-linearly and are first separated by a common dipole that bends all passes toward the side of the tunnel with more available space (the aisle-side, toward the right from the beam’s perspective). Subsequent shared and individual dipoles continue the separation process. Due to the tight packing, avoiding physical collisions between magnets on adjacent beamlines is a major challenge. A key difficulty of the layout is the handling of the two highest-energy passes. To create sufficient clearance from the lower-energy lines, they are bent in the opposite direction, requiring their orbits to cross over and then cross back to ensure they enter the FFA arc in the correct order (lowest energy on the inside, highest on the outside). This would not be necessary if the total number of FFA passes was reduced from six to five, as the beam trajectories would not cross and need to be uncrossed.

3.3. Time-of-Flight and R_{56} Management

To provide the necessary range of path-length adjustment, each of the six independent beamlines incorporates at least one large chicane. Simple vertical stacking of the chicanes was not possible due to the 2.939 m transverse space limit. Instead, the chicanes are nested within each other, like Matryoshka dolls. To further enhance operational flexibility, especially for the lowest-energy pass, smaller “mini-chicanes” are included in series with the main chicane.

To accommodate regular and seasonal path-length changes (which are normally controlled in the doglegs in the current CEBAF machine, but in extreme cases the RF frequency can be adjusted), the design allows for the potential inclusion of mechanical movers on the central dipoles of each chicane. As demonstrated at CBETA, such a system allows for continuous adjustment of the chicane amplitude, providing fine control over the ToF. Figure 2 shows graphically how these mechanical movers may work, if needed.

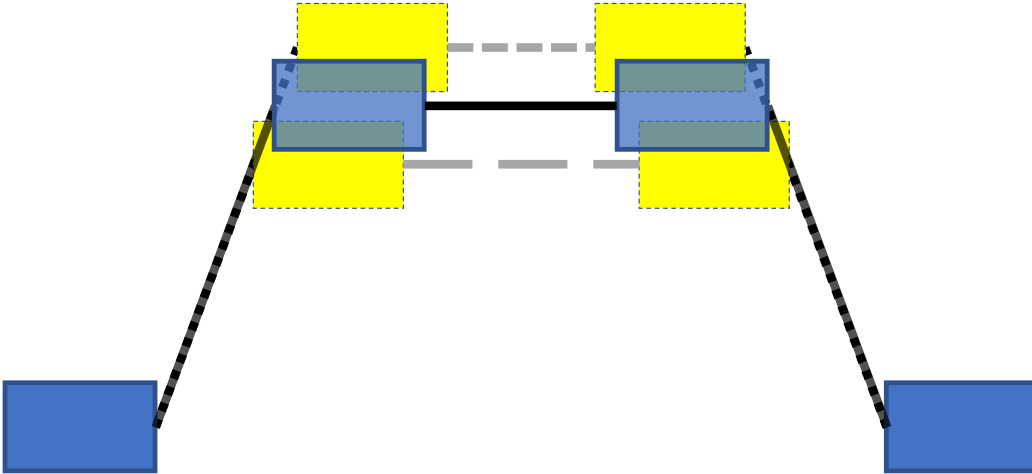


Figure 2: Diagram of the proposed mechanical movers that may or may not be required for path length correction.

R_{56} adjustments must also occur in the splitters. However, the final R_{56} values are still unknown, as parts of the machine are still under design. The largest unknown contributor to the R_{56} that will require compensation in the splitters is the transition section, which is meant to recombine and match the beams from the FFA Arc into the recombiner and LINAC [26, 27]. Currently, ~ 15 m are reserved for the transition section. Recent design progress [27] indicates that the required space is more likely to be around 50 m. Since the length and contribution of this section (and others) are not currently known, only the contributions from the known sections are included in the R_{56} compensation features of the splitters. These values are considered a preliminary “soft target” R_{56} value to be used until the design is finished, and then re-matching will be required.

3.4. Recombination and Matching Section

After discussions with CEBAF Operations crew, and investigations into beam loss and optics complications in the current CEBAF machine, a symmetric recombination scheme using common dipoles was rejected in favor of an independent recombination and matching section for each pass. One of the main rationales for this is the beam loss that CEBAF currently experiences in the recombiner regions, which uses common dipoles to recombine separate energy lines.

This separate-beamline approach, while requiring more magnets, offers superior operational flexibility. It decouples the matching of each pass from the others and provides a dedicated section at the end of most lines. This final section is critical for placing the quadrupoles needed for the final, precise optics match into the FFA arc. It also allows for finer adjustment and matching into the FFA Arcs, including the requirement of non-collinear recombination of the beams. While a symmetric design may be possible, it will lack the operational robustness and flexibility of the design presented here.

3.5. Overall Floor Plan

The complete geometric layout, accommodating all six passes from the common entrance to their individual entry points into the FFA arc, is shown in Figure 3. The reader should note that the axes are not equal, but expanded to show more details of the design. The layout includes all transport dipoles (blue), quadrupoles (red), and extraction dipoles/septa (orange), while respecting all physical boundaries and reserving space for correctors, diagnostics, auxiliaries, and other non-optics beamline components. Stay-clear markers are used with the quadrupoles and extraction dipoles/septa to ensure no encroachment by other elements in that beamline. No elements are in contact with any other elements, though one must zoom in to see the separation in some cases. Also, the final dipoles will likely require chamfering to reduce the corners overlapping with the beamline. Figure 4 shows the location of the splitters in the CEBAF enclosure, scaled appropriately.

4. Optics Design and Matching

4.1. Simulation Framework

All optics simulations were performed using Bmad [24]. The code's ability to model multiple, interacting beamlines was essential. To ensure geometric

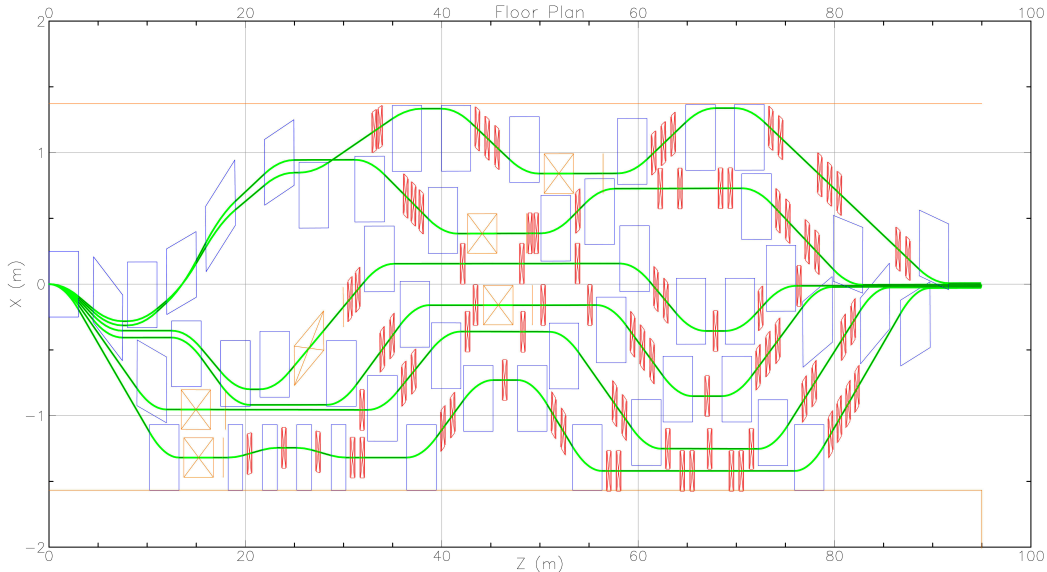


Figure 3: Overhead view of splitter floor plan. Note unequal scales. Dipoles (blue), extraction dipoles (orange), and quadrupoles (red) shown with real dimensions. Horizontal orange lines show transverse spatial limitations with the physical wall at the top and the walkway at the bottom. The aisle-side wall is not shown in this image. Beam travels left to right.

accuracy for the rectangular dipoles used in the design, the “patch method” was employed. This technique uses coordinate system transformations at the entrance and exit of each bend to correctly preserve the magnet geometry, as well as ensure magnets from neighboring beamlines do not collide.

4.2. Matching Strategy

The primary challenge of the optics design is to simultaneously satisfy the multiple matching constraints at the FFA arc entrance. The large dispersion generated by the initial separation chicane, which is often of the wrong sign for matching, proved particularly difficult to correct.

After setting the geometry with the dipoles and adjusting for ToF, the matching process is essentially decoupled from the transport dipoles. Their values are held constant, and only the strengths of the quadrupoles are adjusted. It is important to note that all of the matched solutions that follow only vary the quadrupole strengths: the longitudinal positions are not varied unless otherwise stated. This means that future matches can also start adjusting the placement of the quadrupoles to simplify the process, if needed.

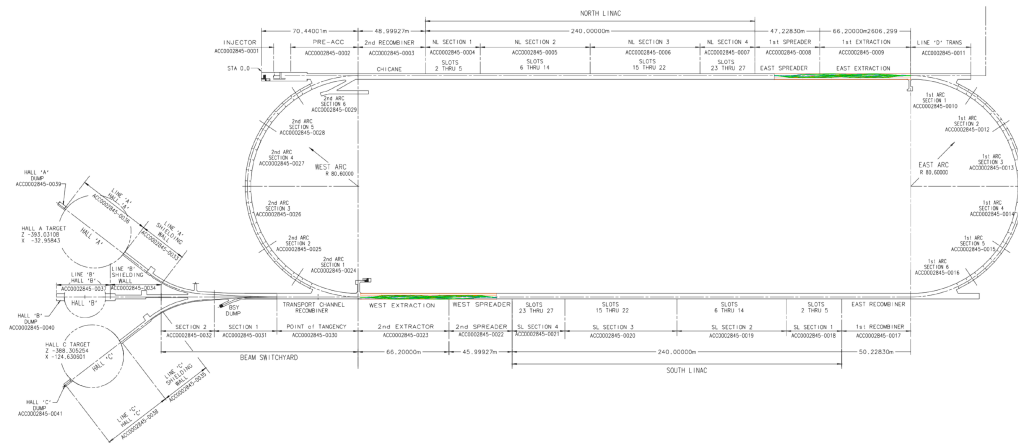


Figure 4: Splitters shown in place in the CEBAF engineering diagram, scaled appropriately. They are located in the northeast and southwest corners. North is up in this image.

But for the work presented here, only the K1 values are adjusted for matching.

All of the limits placed on the quadrupoles are also conservative. K1 values are limited to $\pm 0.6 \text{ m}^{-2}$ in the northeast corner to allow for adequate overhead of the magnets. It also allows for scaling of the quadrupole strengths for the southwest corner, where the beams will transit one additional LINAC and have $\sim 1 \text{ GeV}$ higher-energy beams at each pass.

To demonstrate the robustness of the geometric layout and explore a wider solution space, a strategy was developed to find multiple distinct matching solutions. This was achieved by varying two key sets of assumptions:

1. **LINAC Input Conditions:** Solutions were generated using input matching beam parameters from both LINAC designs under consideration for the upgrade: the weakly focusing triplet (WFT) and strongly focusing triplet (SFT) optics. The WFT optics use realistic quadrupole strengths in the triplets between the cryomodules in the LINAC, but the β -functions end up much larger before the splitters (in the hundreds of meters). The SFT optics uses quadrupole settings that are unrealistically strong, and while attempts at addressing this are ongoing, no solutions have yet proven to be feasible. However, the β -functions exiting the SFT are smaller than those of the WFT, and so provide provide a range of input Twiss parameters from the LINAC into the splitters for matching. This helps to demonstrate the robustness and flexibility

of the splitter design.

2. **FFA Cell Match Point:** To find more tractable solutions, several distinct matching points within the first FFA cell were chosen as targets. Each magnet in the FFA cell is broken into longitudinal sections, and any of those separations can be used as the match point from the splitters into the FFA arc. The primary points investigated were the very beginning of the cell (labeled “Beginning”) and a point of symmetry roughly halfway through the first magnet in the cell, a bending-defocusing magnet (labeled BDC for Bending-Defocusing Center). Figure 5 shows an FFA cell, with the segments and drift spaces indicated in the floor plan and the lattice layout elements of the plot. As shown in Tables 3 and 4, the “BDC” location is advantageous as the α values are nearly zero and the β -functions are at local extrema, simplifying the matching problem. This also allows demonstration that the splitter design is capable of matching into a variety of different FFA designs, which is important, as the FFA arc design is likely to be updated and changed.

Table 3: Comparison of orbit and dispersion target matching parameters for all six east FFA Arc passes.

Pass (E)	Match Point	X (m)	Px	η (m)	η'
1 (10.55 GeV)	Beginning	$-4.3609 \cdot 10^{-2}$	$1.5555 \cdot 10^{-2}$	$1.3845 \cdot 10^{-2}$	$-2.7713 \cdot 10^{-3}$
	BDC	$-3.1036 \cdot 10^{-2}$	$-1.4007 \cdot 10^{-7}$	$-7.8352 \cdot 10^{-3}$	$4.3951 \cdot 10^{-8}$
2 (12.95 GeV)	Beginning	$-4.0953 \cdot 10^{-2}$	$1.4756 \cdot 10^{-2}$	$3.4001 \cdot 10^{-2}$	$-1.1549 \cdot 10^{-2}$
	BDC	$-3.0635 \cdot 10^{-2}$	$-1.7647 \cdot 10^{-7}$	$1.4456 \cdot 10^{-2}$	$-1.8690 \cdot 10^{-7}$
3 (14.95 GeV)	Beginning	$-3.6297 \cdot 10^{-2}$	$1.3082 \cdot 10^{-2}$	$5.0554 \cdot 10^{-2}$	$-1.8809 \cdot 10^{-2}$
	BDC	$-2.8009 \cdot 10^{-2}$	$-1.8064 \cdot 10^{-7}$	$3.2967 \cdot 10^{-2}$	$-3.7558 \cdot 10^{-7}$
4 (17.15 GeV)	Beginning	$-2.9986 \cdot 10^{-2}$	$1.0682 \cdot 10^{-2}$	$6.4348 \cdot 10^{-2}$	$-2.4885 \cdot 10^{-2}$
	BDC	$-2.3526 \cdot 10^{-2}$	$-1.6090 \cdot 10^{-7}$	$4.8495 \cdot 10^{-2}$	$-5.3096 \cdot 10^{-7}$
5 (19.35 GeV)	Beginning	$-2.2289 \cdot 10^{-2}$	$7.6691 \cdot 10^{-3}$	$7.5975 \cdot 10^{-2}$	$-3.0021 \cdot 10^{-2}$
	BDC	$-1.7479 \cdot 10^{-2}$	$-1.4009 \cdot 10^{-7}$	$6.1641 \cdot 10^{-2}$	$-6.6020 \cdot 10^{-7}$
6 (21.55 GeV)	Beginning	$-1.3418 \cdot 10^{-2}$	$4.1373 \cdot 10^{-3}$	$8.5873 \cdot 10^{-2}$	$-3.4401 \cdot 10^{-2}$
	BDC	$-1.0103 \cdot 10^{-2}$	$-1.4475 \cdot 10^{-7}$	$7.2865 \cdot 10^{-2}$	$-7.6926 \cdot 10^{-7}$

For each of these conditions, matching was performed first without considering R_{56} , and then again with R_{56} included as a “soft target.” As a reminder, the R_{56} term is considered a soft target because significant sections are missing which contribute to the values which must be compensated by the splitters. The largest of these is the transition section [26, 27], which

Table 4: Comparison of Twiss target matching parameters (β and α) for all six east FFA Arc passes.

Pass (E)	Match Point	β_x (m)	α_x	β_y (m)	α_y
1 (10.55 GeV)	Beginning	4.1508	3.0414	6.5160	-3.1904
	BDC	$6.6586 \cdot 10^{-1}$	$4.3124 \cdot 10^{-5}$	$1.2039 \cdot 10^1$	$-1.1741 \cdot 10^{-4}$
2 (12.95 GeV)	Beginning	2.9513	1.8208	6.4812	-3.0391
	BDC	1.1641	$2.6829 \cdot 10^{-5}$	$1.0662 \cdot 10^1$	$-1.0407 \cdot 10^{-4}$
3 (14.95 GeV)	Beginning	2.7191	1.5387	7.0035	-3.2108
	BDC	1.3998	$2.4658 \cdot 10^{-5}$	$1.0689 \cdot 10^1$	$-1.0462 \cdot 10^{-4}$
4 (17.15 GeV)	Beginning	2.6034	1.3996	8.0521	-3.6443
	BDC	1.5386	$2.4713 \cdot 10^{-5}$	$1.1607 \cdot 10^1$	$-1.1455 \cdot 10^{-4}$
5 (19.35 GeV)	Beginning	2.5224	1.3113	$1.0173 \cdot 10^1$	-4.5685
	BDC	1.6261	$2.5401 \cdot 10^{-5}$	$1.4063 \cdot 10^1$	$-1.3987 \cdot 10^{-4}$
6 (21.55 GeV)	Beginning	2.4564	1.2473	$1.7058 \cdot 10^1$	-7.6233
	BDC	1.6824	$2.6113 \cdot 10^{-5}$	$2.2819 \cdot 10^1$	$-2.2893 \cdot 10^{-4}$

will likely take up far more longitudinal distance than is currently assumed by the available space. But matching without the R_{56} will show one set of solutions, and then using a soft target R_{56} to see what Twiss parameters must be sacrificed helps to bound what the final solutions will likely need to be. It also shows if any changes should be made to the FFA arc design to alter their R_{56} contributions.

4.3. Presentation of Results

Thus far, six sets of matching solutions have been proven successful, demonstrating the viability and flexibility of this splitter design. These six solutions can be broken into three pairs of solutions. Each pair consists of one solution which matches all of the Twiss parameters but ignores R_{56} compensation, and one solution which compensates for a “soft target” R_{56} and most of the Twiss parameters. This section will present some of these solutions, as well as compare them.

Only one example of each match will be shown in the main body of this text. However, for completeness the reader is encouraged to see A for plots, match parameter tables, and quadrupole strength tables for all six of the match solutions.

4.3.1. Match Without R_{56} Compensation

When ignoring the R_{56} constraint, all other optics parameters can be matched successfully for all six passes. The resulting β -functions and dis-

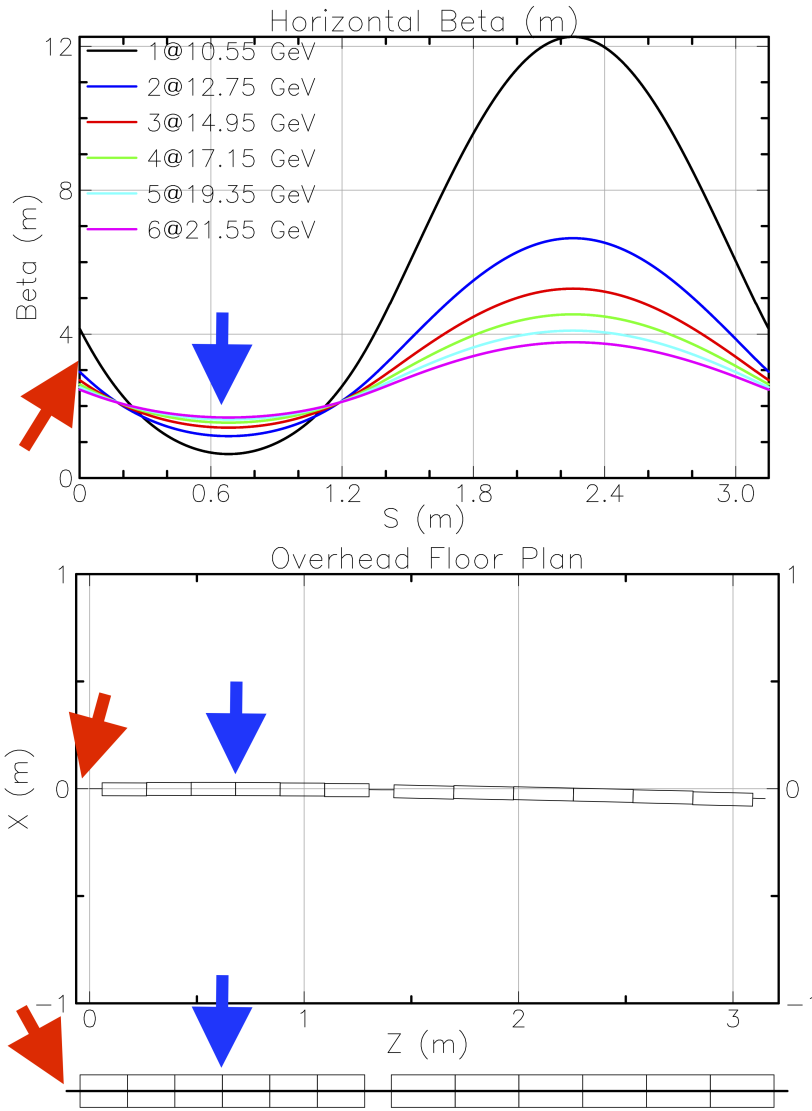


Figure 5: An FFA Cell, including the segmented Bending-Defocusing (left) and Bending-Focusing (right) magnets. β -functions for each energy pass shown. The match points used for this work are at the beginning of this cell (far left, at the drift indicated by the red arrows), and in the center of the first magnet (after three segments in the first magnet, indicated by the blue arrows).

person along the splitter are well-behaved. Though β -functions can become large, they are within the expected requirements of the beamline. All

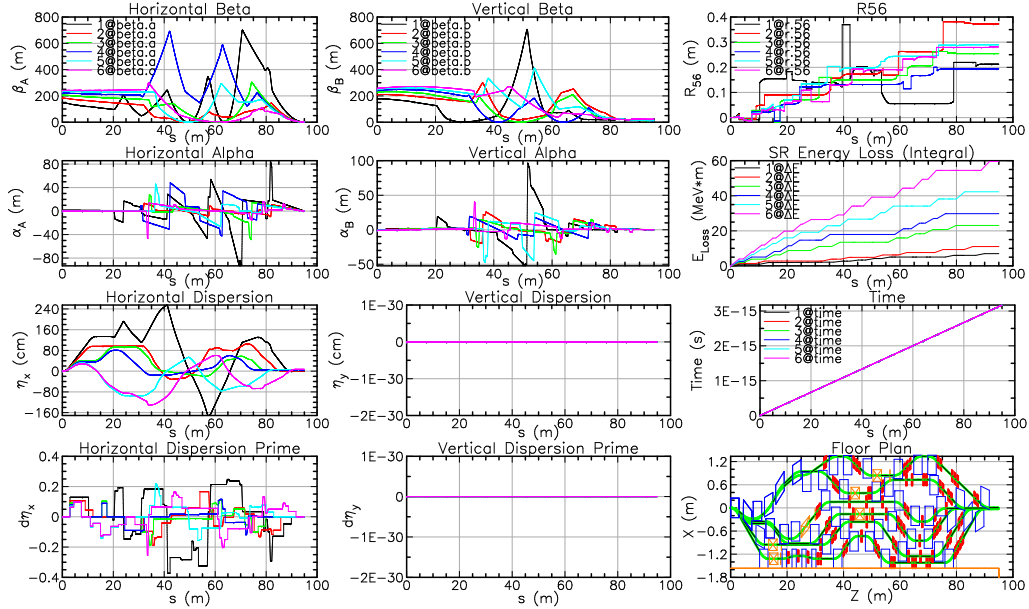


Figure 6: Matching solution from the WFT LINAC input into the BDC FFA match point. In this case, all of the Twiss parameters are matched to within machine precision, and R_{56} compensation is ignored.

quadrupoles were limited to K1 values of 0.6 m^{-2} to leave adequate overhead, and allow for scaling of the solution to the southwest corner splitter, which will have higher energies. Plots for the various match parameters are shown in Figure 6 for the case of the WFT LINAC input optics being matched into the BDC match point in the FFA Cell.

The merit function for all of the match parameters are effectively zero for all six passes (A.1.2), indicating a near-perfect match (Table 10). The quadrupole strengths are all at or below the enforced limits (Table 11). The maximum β -functions are within the 700 m limit placed upon the optimizer.

4.3.2. Match With R_{56} as a “Soft Target”

Including the R_{56} constraint significantly complicates the problem. The strong quadrupole fields needed to alter the dispersion and R_{56} create large perturbations in the β -functions. While solutions have been found that bring the R_{56} close to the target value, this often comes at the cost of compromising the match of other parameters.

Figure 7 shows the match solutions for all six passes from the WFT

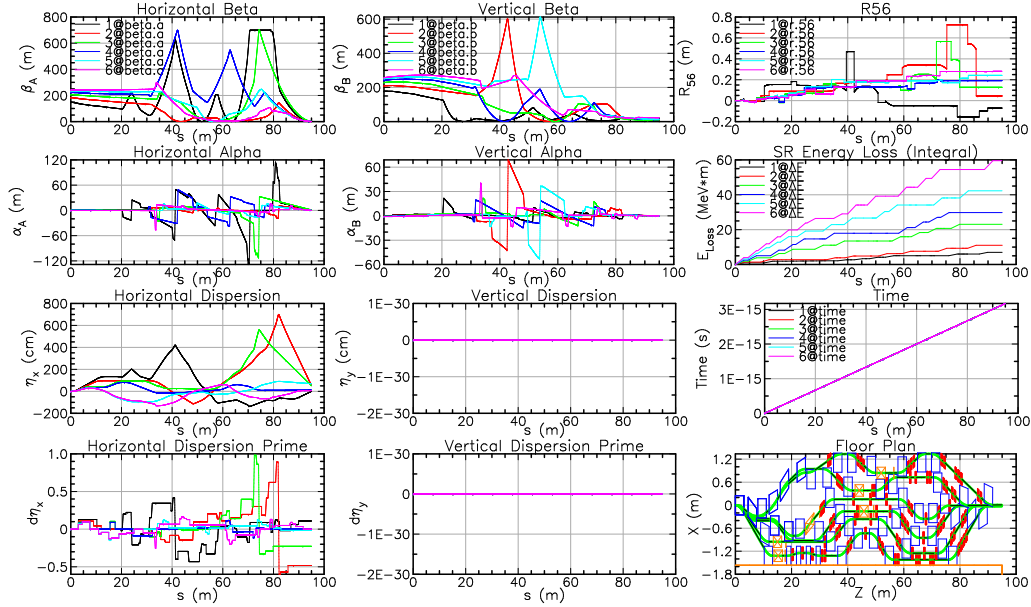


Figure 7: Matching solution from the WFT LINAC input into the BDC FFA match point. In this case, R_{56} and $\beta_{x,y}$ is always matched perfectly, $\alpha_{x,y}$ usually matched very well or perfectly, and η_x and η'_x are matched adequately.

LINAC input into the BDC match point in the FFA cell. The tables in A.2.2, specifically Tables 16 and 17, show the merit functions for all of the match parameters, and the quad strengths required to achieve said matches, respectively. In order to achieve these matches and compensate R_{56} , some small sacrifices were made in other match parameters. Specifically, the horizontal η and η' matches were de-prioritized, and for the third pass, the $\alpha_{x,y}$ match was not as strong. The merit functions for nearly all other parameters are effectively zero.

4.3.3. Comparison of Solutions

The existence of multiple solutions under different input conditions (WFT vs. SFT) and for different match points (Beginning vs. BDC) confirms that the geometric design is not rigidly tied to a single, unique solution. This inherent flexibility is crucial for the success of the overall machine upgrade, as other components of the accelerator are still being designed. Furthermore, this demonstrated robustness will translate to greater operational flexibility and ability to match for non-nominal beams which tend to be the normal

operating state of CEBAF.

For the two inputs, there is not a large difference for the results of the matching: the splitters are able to match from both LINAC input options. It could be argued that the Weakly Focusing Triplet option allows for matches which more easily control the maximum β -functions during transport, but this is only a minor point. In all cases, the maximum β -functions during transport correspond to beam sizes which fall within the 10σ beam-stay-clear (BSC) limits of CEBAF. Please see B for further details on this.

More weight depends upon the match point in the FFA Cell. Here, it is very clear that the BDC match point is far simpler for matching, with more solutions being achieved here, and with lower overall merit functions. Further investigations into other FFA Cell match points may find even better options. Additionally, the FFA Arc design is under flux, and it may be that improved solutions can be discovered as the overall design evolves.

Nonetheless, with two very different input and output options, this splitter design is capable of matching all of the optics parameters, or some of the optics parameters and R_{56} compensation. The two best options are those shown in the text above. However, these are both based upon the WFT input option, which is not currently the assumed baseline for the energy upgrade.

A brief comparison of the merit functions of the six solutions is shown in Table 5. For more details of the matches, including tables showing all of the match parameters, target values, achieved values, and merit functions, please see A. This also includes a brief description of how Bmad and Tao calculate the merit functions.

4.4. Discussion of Optics Challenges

While the design of this splitter is robust and flexible, there are some remaining challenges. This section will describe some of the challenges.

4.4.1. Magnet Crosstalk and Fringe Fields

When looking at the floor plan of this design, it is reasonable to have concerns with the tight-packed nature of the layout. While no elements are in contact with other elements, they are very close in proximity, and the fields of the magnets will influence the beams in adjacent beamlines. This concern is valid and needs to be fully investigated, along with other error analysis.

Table 5: Quantitative comparison of the six matching solutions, demonstrating the flexibility of the geometric design. The 'Merit Function Range' quantifies the final match quality, where a lower value indicates a better match. For the 'No R_{56} ' cases, the R_{56} merit is excluded from this range to show the intended match quality. The data illustrates that matching R_{56} (bottom half) consistently requires sacrificing the dispersion (η_a) match. The solutions shown in **bold** are those presented as primary examples in Section 4.

Solution (Input → Match Point)	R_{56} Matched	Merit Function Range	Primary Sacrificed Parameters
SFT → Beginning	No	$0 \rightarrow 5.76 \cdot 10^5$	$\max(\beta_a), \max(\beta_b)$
SFT → BDC	No	≈ 0	None (All merits ≈ 0)
WFT → BDC	No	≈ 0	None (All merits ≈ 0)
SFT → Beginning	Yes	$0 \rightarrow 1.40 \cdot 10^9$	$\eta_a, \alpha_b, \eta'_a$
SFT → BDC	Yes	$0 \rightarrow 4.06 \cdot 10^8$	$\eta_a, \alpha_b, \eta'_a$
WFT → BDC	Yes	$0 \rightarrow 4.06 \cdot 10^7$	η_a, η'_a

However, this is also a problem that is very familiar to CEBAF Operations. In fact, our spreaders, recombiners, and extraction regions all manage multipass beamlines with very tight tolerances. Figure 8 shows several examples of such tight clearances in the current CEBAF machine. Figure 8a shows a lower-energy beam pipe passing through the return steel of a common dipole, while remaining outside of the coils. This is also a good example of what this splitter design aims to avoid: recombining beamlines through a common dipole. Figure 8b shows a spreader dipole with a lower-energy pass touching and running along the top of it, with some magnetic shielding placed between the beam pipe and the magnet steel. Figure 8c shows a very small gap of ~ 1.5 cm between the return steel of dipoles from adjacent beamlines. Figure 8d shows three beamlines of different energies installed within approximately 20 cm from each other, with the middle of these running along the quadrupole return steel from an adjacent line.

The point of displaying these photographs is to demonstrate that, while close proximity of adjacent beamlines to each other is not ideal, it is a common occurrence at CEBAF: one that the Operations crew has the knowledge and experience to accommodate during beam operations. Judicious use of corrector magnets, as well as startup and adjustment procedures (such as magnet hysteresis cycling) allows for strong and accurate control of each energy beam. By ensuring that the crosstalk is reproduced and repeatable, operations can ensure that the steering contribution is consistent.

Furthermore, different choices in magnetic shielding and beam pipe material can reduce the impact of stray fields on adjacent beamlines. For example, carbon steel beam pipes can adequately shield against stray fields. If more shielding is required, a layered/jacketed beamline can also be used. If there is adequate space, magnetic shielding can also be installed between beamlines to further reduce the impact.

Also, should the decision be made to reduce the number of energies transiting the FFA be reduced from six to five, the physical constraints would be reduced for the splitters, and the elements from each adjacent line would be allowed more space.

4.4.2. *Dispersion Control*

Controlling the dispersion of all six beamlines is also challenging. Separating the beamlines requires large, strong bending dipoles. Given the rigidity of the beams, there is not adequate space for placement of independent quadrupoles for several tens of meters into the beamline. In this space, the dispersion due to the bends is uncompensated, and the β -functions are uncontrolled. Furthermore, the space constraints necessitate bending the beams in a direction which creates dispersion that is counter to what is needed upon entry into the FFA arcs. This combination of factors necessitates strong quadrupoles to be used for dispersion control and Twiss parameter matching.

To include extraction of the beams (see Section 5), dipoles and/or septa need to be installed early in each line as well. They must happen early to allow adequate space for the transfer lines from the splitters to the extraction lines themselves. This further delays placement of quadrupoles.

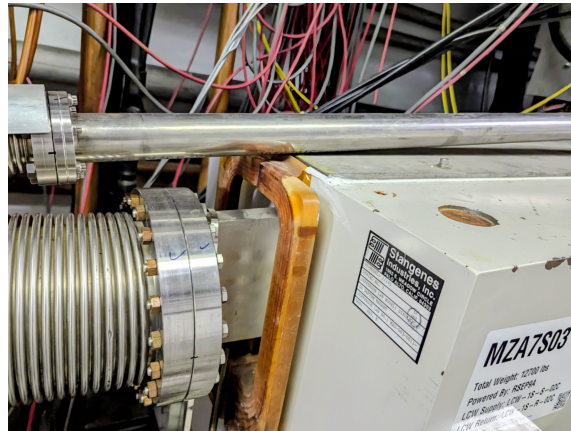
The final target values for ToF and R_{56} depend on the design of the downstream transition section, which is not yet complete [26, 27]. Compensating for the R_{56} and matching the Twiss parameters is further complicated by including dispersion matching. In the matches above, sacrificing the quality of the match for η and η' tends to allow for matching all of the other parameters. Once the transition section design is finalized, the splitter optics will need to be re-matched in an iterative process with the FFA arc design to reduce the matching burden on the splitter.

4.4.3. *Energy Loss and Emittance*

For any high energy transport line, beam degradation due to synchrotron radiation needs to be examined. For the designs presented, this was done by



(a) Beam pipe through return steel of common dipole.



(b) Dipole MZA7S03 with beamline along top.



(c) 1.5 cm gap between dipoles.



(d) Three beamlines within ~ 20 cm .

Figure 8: Several photographs of CEBAF beamlines with tight clearances.

using radiation integrals to calculate beam loss, increase in energy spread, and increase in emittance. The relevant radiation integrals for a transfer line are given below:

$$\begin{aligned}
L_2 &= \int g^2 \gamma_0^4 ds \\
L_3 &= \int g^3 \gamma_0^7 ds \\
L_{5x} &= \int g^3 \mathcal{H}_x \gamma_0^6 ds,
\end{aligned}$$

where $g = 1/\rho$, with ρ being the radius of curvature, γ_0 being the relativistic factor, and $\mathcal{H}_x = \gamma_x \eta_x^2 + 2\alpha_x \eta_x \eta'_x + \beta_x \eta_x'^2$, the curly H function. The energy loss, increase in energy spread, and increase in normalized emittance is then given by

$$\begin{aligned}
U_0 &= \frac{2}{3} r_c m c^2 L^2 \\
\sigma_E^2 &= \frac{4}{3} C_q r_c (m c^2)^2 L_3 \\
\epsilon_{nx} &= \frac{2}{3} C_q r_c L_{5x}
\end{aligned}$$

where r_c is the classical electron radius, m is the mass of the electron, c is the speed of light, and $C_q = \frac{55}{32\sqrt{3}} \frac{h}{mc}$ [28, 29].

The energy loss and increase in energy spread for a given splitter line is constant for the solutions presented, depending only on the dipole strengths. While larger than desired, they remain within a range that is typical for high-energy transport lines in constrained geometries. While the induced energy spread will require careful management in the experimental halls, it does not present a fundamental barrier to beam transport. The only way to minimize either of these considerations is by reducing the dipole bend angle, which would require either fewer splitter lines or a larger footprint.

The emittance growth is substantial, with the final emittance after transport through all six lines being one or two orders of magnitude larger than desired, depending on the solution; this is a natural consequence of the large \mathcal{H} -function values through the strong bends required by the constrained footprint. The emittance growth is not spread equally over a given splitter line: while two equal bends will contribute equally to the energy loss, the optics through the dipoles, i.e., the \mathcal{H} -function through the dipoles, can mean that one of the two dipoles is the primary driver in emittance growth, while the

other is almost negligible. Thus, when considering how to minimize emittance growth for a future design iteration, both bend strengths and optics must be taken into consideration. It may be more fruitful to reduce the bend strength of select dipoles, instead of reducing the bends of all dipoles equally. This becomes even more critical for the first and last dipole in each line; given the fixed optics at both ends of the beamlines, the only real lever at these locations to reduce L_{5x} is the dipole bend strength. However, with sufficient relaxation in requirements and flexibility in optics match parameters, this may be a problem that can be solved in future iterations.

Furthermore, given the number of variables and constraints that are considered in this overall design, it was deemed a higher priority to focus on those previously described parameters. Once more of the Energy Upgrade design is complete, including the FFA arcs, the LINACs, and the transition sections, rematching of the splitters will be required. At this time, the lines can be properly optimized to include reduction of emittance growth.

5. Beam Extraction Scheme

5.1. Rationale for Extraction from the Splitter

The splitter is the only location in the FFA@CEBAF design where the high-energy passes are physically separated by a significant distance. This makes it the only feasible location for installing a system to extract these beams and deliver them to the experimental halls. Therefore, incorporating an extraction scheme was a core requirement of the design. This splitter design is the only one which includes extraction capabilities.

5.2. Conceptual Design

The proposed extraction system reserves space in each of the six beamlines for a 3 m-long C-dipole or septum magnet. This allows for two potential modes of operation:

1. **Magnetic Extraction:** By powering the extraction magnet in a given pass, the beam would be bent vertically downwards towards a transfer line leading to the Beam Switchyard (BSY). This method would likely send the same energy beam to Halls A, B, and C simultaneously, while Hall D operates separately.

2. **RF-Kicker Extraction:** A timed vertical kick from an upstream RF kicker could be used in conjunction with the septa to extract individual beam bunches from a specific pass, offering more flexibility. This concept is under further investigation [30].

5.3. Integration into the Layout

The extraction dipoles are placed within the main chicanes of each beamline, as shown by orange rectangles in the floor plan (Figure 3). This placement represents a compromise, as it occupies space that could otherwise be used for quadrupoles. However, by placing them on the upstream side of the main chicane, the downstream matching section remains clear for final optics control.

6. Summary and Future Work

6.1. Summary of Accomplishments

This work has produced a complete, detailed, conceptual design for a horizontal splitter for the FFA@CEBAF energy upgrade. The design successfully fits all necessary magnetic elements and beam trajectories within the severe physical constraints of the CEBAF tunnel. The robustness of the design has been demonstrated by finding multiple viable optics matching solutions under a variety of input conditions. Finally, the design incorporates a feasible plan for high-energy beam extraction, a critical requirement for the facility's physics program. It remains the only current solution that provides both multiple matching options and beam extraction capability.

6.2. Future Work and Refinements

While this conceptual design is a major step forward, significant work remains.

- **Optics:** The immediate next step is to rematch the optics once the downstream transition section design is finalized and the definitive target values for ToF and R_{56} are known. Future optimization studies will also explore varying the longitudinal placement of the quadrupoles, in addition to their strengths, to access a larger solution space and potentially find more robust and efficient matches. Changes to the FFA arc match conditions, as the design evolves, will also be required.

Given the complexity of this system, error analysis will be required. Specifically, the sensitivity to off-momentum and misalignments must be studied. Chromaticity should be investigated as well, given the size of the β -functions in some of the matches. Magnet error sensitivities will also need to be investigated. Eventually, particle tracking will also need to be completed to study beam loss and aperture limitations.

Depending on the complexities of matching solutions once the transition section and the FFA Arc updates and changes are completed, it may necessitate the use of multifunction magnets. The authors do not think they will be necessary, but it is worth investigating their use to simplify the overall design and quantify their impact on the overall design.

- **Engineering:** Detailed engineering studies are required to refine the design. While first-order considerations have been addressed, further investigation is needed regarding magnet good-field regions, cross-talk between closely interleaved magnets, and proximity to beamline infrastructure such as pumps, valves, and cabling. Fringe and stray-field mitigation will also be necessary.
- **Performance:** Further beam dynamics studies are needed to evaluate the splitter's impact on beam quality, particularly concerning emittance growth from synchrotron radiation, and to establish error tolerances for magnet misalignments and field errors.

6.3. Potential Simplifications

The complexity of the six-pass design is significant. Most of the complexity is due to the physical space constraints. One way that this could be alleviated would be to extend the space to include the whole width of the tunnel, and using ramps to allow for equipment to pass over the beamlines. The ramps would need to be capable of holding the weight of very heavy equipment, such as cryomodules, as well as have a low enough angle to allow for heavy equipment to be rolled over the ramps. One would also need to use caution, as the ceiling may present oxygen deficiency hazards (ODH), and the heads of personnel may be in ODH hazards of higher risk.

Many of the challenges related to component spacing and interleaved magnets would be substantially mitigated by reducing the number of FFA passes from six to five. This option would create valuable additional space,

simplify the overall design, and likely reduce the synchrotron energy loss and emittance growth, and should be considered as the overall design of the FFA@CEBAF upgrade matures. The authors believe that this reduction of the total number of passes is more appropriate.

7. Acknowledgments

Authored by Jefferson Science Associates, LLC under U.S. DOE Contract No. DE-AC05-06OR23177.

Thanks to all who contributed, especially those in CEBAF Operations, who provided insights into the operational complications that come with such a design and suggestions to improve. Special thanks to Scott Berg, who provided the initial recipe for this design based upon his work at CBETA, as well as significant amounts of advice and guidance. Thanks to Todd Satogata and Yves Roblin, who provided meaningful advice and recommendations of the work.

A. Matching Parameters

For completeness, all matching parameters, merit functions, and quadrupole settings for each of the six solutions will be included in this section, as well as relevant plots. There are two main sections, one describing match solutions without the "soft target" R_{56} compensation, and another which sacrifices some Twiss matching to compensate for the R_{56} . Within each of those sections, it is further broken down into which input conditions are being used: the Strong Focusing Triplet (SFT) LINAC or the Weakly Focusing Triplet (WFT) LINAC. Finally, there may be separate solutions within a section of the above categories, which will be indicated.

With regards to the merit function numbers, the goal is to minimize these values. They are calculated by the Tao simulation program part of Bmad [31], and related to the values of the data (targets) and variables, and the weights placed upon the variables. These weights are sometimes adjusted manually by the user in efforts to guide the simulations toward specific goals. For this reason, the authors are including the targets for each match and the model values as well, so that the combination of these and the overall merit function can describe the quality of the matches. Most simply, a smaller the merit function indicates a better match. However, the combination of the variable and target values, as well as the weights of the final matches will influence how low the merit functions may be able to achieve.

A.1. Matches Without R_{56} Compensation

The following will show match solutions without the inclusion of R_{56} compensation. They are broken apart by input LINAC optics; either from the SFT or WFT.

A.1.1. Strong Focusing Triplet LINAC Input

There are two matches which use the SFT as inputs: one from SFT into the Beginning match point in the FFA Cell, and another from SFT to the BDC match point in the FFA Cell. Both are shown below, and the reader is requested to take care when reading the following tables.

Showing first the SFT matching into the Beginning FFA Cell match point:

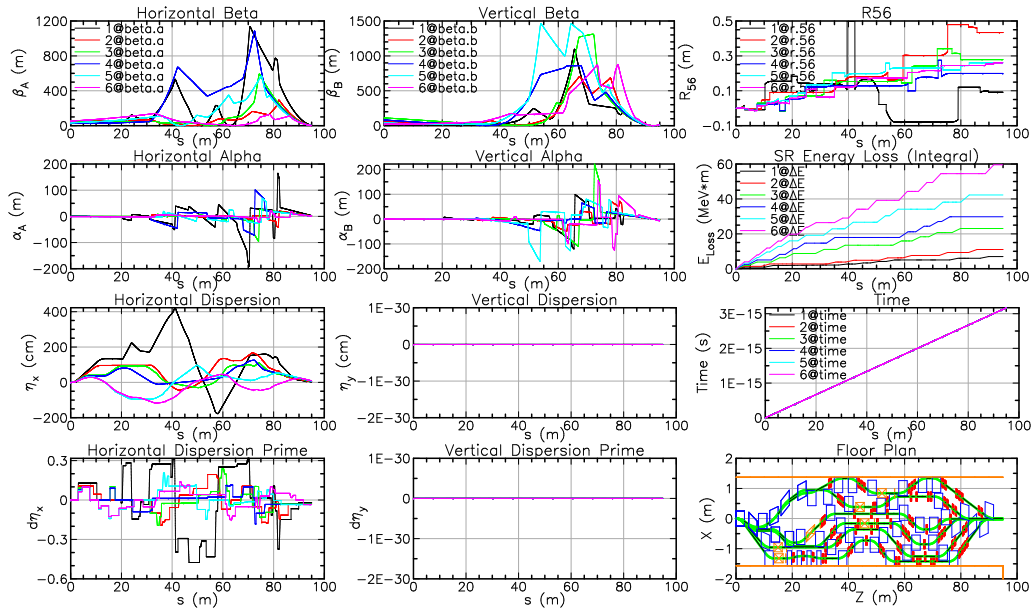


Figure 9: Matching solution from the SFT LINAC input into the Beginning FFA match point. In this case, all or nearly all of the Twiss parameters are matched well, and R_{56} compensation is ignored.

Table 6: Complete summary of Twiss parameter optimization constraints for the matching case of the SFT LINAC input and the Beginning match point in the FFA Arc, excluding R_{56} matching. This includes target values for optical functions at the beamline end-point and maximum value limits throughout the line for each of the six energy passes.

Parameter	Target/Limit	Model Value	Merit	Location
First Pass				
β_a [END]	4.1573×10^0	4.1573×10^0	9.373×10^{-7}	-
β_b [END]	6.5151×10^0	6.5151×10^0	2.916×10^{-7}	-
α_a [END]	3.0489×10^0	3.0489×10^0	7.836×10^{-8}	-
α_b [END]	-3.1896×10^0	-3.1896×10^0	5.412×10^{-8}	-
η_a [END]	2.7200×10^{-2}	2.7200×10^{-2}	1.883×10^{-11}	-
η'_a [END]	-1.9800×10^{-2}	-1.9800×10^{-2}	9.289×10^{-13}	-
R_{56} [END]	-7.0886×10^{-2}	9.1707×10^{-2}	2.644×10^{13}	-
$\max(\beta_a)$	7.0000×10^2	1.1342×10^3	1.885×10^5	M9Q16
$\max(\beta_b)$	7.0000×10^2	1.0804×10^3	1.447×10^5	M9Q14
Second Pass				
β_a [END]	2.9506×10^0	2.9506×10^0	5.130×10^{-16}	-
β_b [END]	6.4768×10^0	6.4768×10^0	2.840×10^{-19}	-
α_a [END]	1.8215×10^0	1.8215×10^0	8.780×10^{-21}	-
α_b [END]	-3.0366×10^0	-3.0366×10^0	5.049×10^{-23}	-
η_a [END]	4.5700×10^{-2}	4.5700×10^{-2}	2.053×10^{-21}	-
η'_a [END]	-2.6400×10^{-2}	-2.6400×10^{-2}	1.157×10^{-22}	-
R_{56} [END]	4.4694×10^{-2}	4.3370×10^{-1}	1.513×10^{14}	-
$\max(\beta_a)$	7.0000×10^2	2.9197×10^2	0	M11Q14
$\max(\beta_b)$	7.0000×10^2	7.0000×10^2	0	D1105#5
Third Pass				
β_a [END]	2.7180×10^0	2.7180×10^0	2.827×10^{-3}	-
β_b [END]	6.9948×10^0	6.9948×10^0	1.848×10^0	-
α_a [END]	1.5388×10^0	1.5387×10^0	1.164×10^{-2}	-
α_b [END]	-3.2063×10^0	-3.2063×10^0	2.432×10^{-3}	-
η_a [END]	6.0800×10^{-2}	6.0800×10^{-2}	3.006×10^{-13}	-
η'_a [END]	-3.0900×10^{-2}	-3.0900×10^{-2}	1.627×10^{-9}	-
R_{56} [END]	1.2809×10^{-1}	2.7849×10^{-1}	2.262×10^{13}	-
$\max(\beta_a)$	7.0000×10^2	5.9036×10^2	0	M13Q12
$\max(\beta_b)$	7.0000×10^2	1.3097×10^3	3.718×10^5	D1308#2

Continued on next page

Table 6: (Continued)

Parameter	Target/Limit	Model Value	Merit	Location
Fourth Pass				
β_a [END]	2.6023×10^0	2.6023×10^0	1.965×10^0	-
β_b [END]	8.0350×10^0	8.0350×10^0	3.452×10^{-2}	-
α_a [END]	1.3995×10^0	1.3995×10^0	1.419×10^{-3}	-
α_b [END]	-3.6359×10^0	-3.6359×10^0	2.086×10^{-4}	-
η_a [END]	7.3500×10^{-2}	7.3500×10^{-2}	1.252×10^{-8}	-
η'_a [END]	-3.3600×10^{-2}	-3.3600×10^{-2}	3.325×10^{-6}	-
R_{56} [END]	1.9190×10^{-1}	1.9951×10^{-1}	5.797×10^{10}	-
$\max(\beta_a)$	7.0000×10^2	1.0755×10^3	1.410×10^5	D1508#2
$\max(\beta_b)$	7.0000×10^2	8.5944×10^2	2.542×10^4	D1507#2
Fifth Pass				
β_a [END]	2.5213×10^0	2.5213×10^0	2.067×10^0	-
β_b [END]	1.0132×10^1	1.0132×10^1	6.994×10^{-1}	-
α_a [END]	1.3111×10^0	1.3111×10^0	1.458×10^{-3}	-
α_b [END]	-4.5492×10^0	-4.5492×10^0	1.077×10^{-3}	-
η_a [END]	8.4100×10^{-2}	8.4101×10^{-2}	3.896×10^{-5}	-
η'_a [END]	-3.4900×10^{-2}	-3.4900×10^{-2}	1.323×10^{-5}	-
R_{56} [END]	2.4233×10^{-1}	2.6042×10^{-1}	3.272×10^{11}	-
$\max(\beta_a)$	7.0000×10^2	5.6689×10^2	0	D1710#5
$\max(\beta_b)$	7.0000×10^2	1.4590×10^3	5.760×10^5	M17Q6
Sixth Pass				
β_a [END]	2.4552×10^0	2.4552×10^0	6.660×10^{-3}	-
β_b [END]	1.6840×10^1	1.6840×10^1	1.409×10^{-2}	-
α_a [END]	1.2471×10^0	1.2471×10^0	1.888×10^{-6}	-
α_b [END]	-7.5245×10^0	-7.5245×10^0	2.055×10^{-5}	-
η_a [END]	9.3200×10^{-2}	9.3200×10^{-2}	5.910×10^{-9}	-
η'_a [END]	-3.5000×10^{-2}	-3.5000×10^{-2}	1.126×10^{-8}	-
R_{56} [END]	2.8081×10^{-1}	2.6071×10^{-1}	4.040×10^{11}	-
$\max(\beta_a)$	7.0000×10^2	1.3979×10^2	0	D1906#2
$\max(\beta_b)$	7.0000×10^2	8.6919×10^2	2.863×10^4	D1912#2

Table 7: Optimized integrated quadrupole strengths (K_1) for each of the six passes. The longitudinal position of the center of each magnet is given by the S-coordinate. All quadrupole strengths were limited to a range of $\pm 0.6 \text{ m}^{-2}$ during the optimization.

Element	S-Pos. (m)	K_1 (m^{-2})	Element	S-Pos. (m)	K_1 (m^{-2})
First Pass (P9) Quadrupoles					
M9Q1	20.66	-0.6000	M9Q11	57.28	0.5811
M9Q2	24.16	0.5405	M9Q12	58.28	0.5347
M9Q3	27.66	-0.1765	M9Q13	64.78	0.0693
M9Q4	31.16	-0.4388	M9Q14	65.78	-0.5702
M9Q5	32.16	-0.0596	M9Q15	69.78	-0.0990
M9Q6	40.36	-0.0980	M9Q16	70.78	0.5675
M9Q7	41.36	0.4725	M9Q17	79.88	-0.4501
M9Q8	46.66	0.2116	M9Q18	80.78	0.3674
M9Q9	51.66	-0.3877	M9Q19	81.68	0.6000
M9Q10	52.66	-0.0463	M9Q20	82.58	-0.6000
Second Pass (P11) Quadrupoles					
M11Q1	32.11	0.2937	M11Q8	63.28	-0.1620
M11Q2	36.36	-0.2157	M11Q9	67.54	-0.2364
M11Q3	37.36	-0.2807	M11Q10	71.80	0.2626
M11Q4	42.86	0.6000	M11Q11	77.21	0.0153
M11Q5	48.50	0.6000	M11Q12	78.21	-0.3844
M11Q6	57.86	0.0721	M11Q13	81.21	-0.2265
M11Q7	58.86	0.2828	M11Q14	82.21	0.6000
Third Pass (P13) Quadrupoles					
M13Q1	34.16	0.5247	M13Q7	60.66	0.1792
M13Q2	35.16	-0.6000	M13Q8	61.66	0.4476
M13Q3	43.66	0.0405	M13Q9	67.28	-0.2390
M13Q4	50.55	0.6000	M13Q10	72.46	-0.4977
M13Q5	55.30	0.6000	M13Q11	73.46	0.0037
M13Q6	59.66	-0.5072	M13Q12	74.46	0.6000
Fourth Pass (P15) Quadrupoles					
M15Q1	30.86	-0.0460	M15Q6	62.04	0.0391
M15Q2	31.66	-0.5962	M15Q7	63.04	-0.0441

Table 7: (Continued)

Element	S-Pos. (m)	K_1 (m ⁻²)	Element	S-Pos. (m)	K_1 (m ⁻²)
M15Q3	42.35	0.2561	M15Q8	68.11	-0.2162
M15Q4	48.36	0.0148	M15Q9	72.70	0.4529
M15Q5	54.05	-0.1609	M15Q10	76.62	-0.2683
Fifth Pass (P17) Quadrupoles					
M17Q1	36.56	0.5500	M17Q8	64.50	-0.2833
M17Q2	37.36	-0.5500	M17Q9	68.63	-0.0718
M17Q3	38.16	0.5088	M17Q10	69.63	-0.0766
M17Q4	49.23	-0.0375	M17Q11	74.48	0.0286
M17Q5	49.87	0.5500	M17Q12	75.48	0.4606
M17Q6	54.09	-0.3913	M17Q13	77.48	-0.5500
M17Q7	62.50	0.3729	M17Q14	78.48	0.2466
Sixth Pass (P19) Quadrupoles					
M19Q1	33.36	0.1070	M19Q9	73.75	-0.0585
M19Q2	33.96	0.0541	M19Q10	74.75	0.0570
M19Q3	43.86	-0.1464	M19Q11	78.75	-0.0251
M19Q4	44.86	-0.1317	M19Q12	79.75	-0.1948
M19Q5	45.86	0.1897	M19Q13	80.75	-0.1513
M19Q6	61.81	0.6000	M19Q14	86.75	0.5286
M19Q7	62.81	0.3166	M19Q15	87.75	-0.0635
M19Q8	63.81	-0.5285			

Showing next the SFT matching into the BDC FFA Cell match point:

Table 8: Complete summary of Twiss parameter optimization constraints for the matching case of the SFT LINAC input and the BDC match point in the FFA Arc, excluding R_{56} matching. This includes target values for optical functions at the beamline end-point and maximum value limits throughout the line for each of the six energy passes.

Parameter	Target/Limit	Model Value	Merit	Location
First Pass				
β_a [END]	6.6586×10^{-1}	6.6586×10^{-1}	2.840×10^{-19}	-

Continued on next page

Table 8: (Continued)

Parameter	Target/Limit	Model Value	Merit	Location
β_b [END]	1.2039×10^1	1.2039×10^1	6.185×10^{-18}	-
α_a [END]	4.3124×10^{-5}	4.3124×10^{-5}	1.180×10^{-21}	-
α_b [END]	-1.1741×10^{-4}	-1.1741×10^{-4}	4.793×10^{-23}	-
η_a [END]	-7.8352×10^{-3}	-7.8352×10^{-3}	1.516×10^{-20}	-
η'_a [END]	4.3951×10^{-8}	4.3951×10^{-8}	1.309×10^{-22}	-
R_{56} [END]	-7.0886×10^{-2}	1.2731×10^{-1}	3.928×10^{13}	-
$\max(\beta_a)$	7.0000×10^2	7.0000×10^2	0	M9Q16
$\max(\beta_b)$	7.0000×10^2	2.0685×10^2	0	D908#2
Second Pass				
β_a [END]	1.1641×10^0	1.1641×10^0	6.390×10^{-19}	-
β_b [END]	1.0662×10^1	1.0662×10^1	3.032×10^{-17}	-
α_a [END]	2.6829×10^{-5}	2.6829×10^{-5}	9.488×10^{-22}	-
α_b [END]	-1.0407×10^{-4}	-1.0407×10^{-4}	5.382×10^{-24}	-
η_a [END]	1.4456×10^{-2}	1.4456×10^{-2}	2.359×10^{-25}	-
η'_a [END]	-1.8690×10^{-7}	-1.8690×10^{-7}	1.007×10^{-22}	-
R_{56} [END]	4.4694×10^{-2}	3.7945×10^{-1}	1.121×10^{14}	-
$\max(\beta_a)$	7.0000×10^2	1.4403×10^2	0	D1106#11
$\max(\beta_b)$	7.0000×10^2	2.5212×10^2	0	D1105#5
Third Pass				
β_a [END]	1.3998×10^0	1.3998×10^0	7.704×10^{-18}	-
β_b [END]	1.0669×10^1	1.0669×10^1	5.834×10^{-17}	-
α_a [END]	2.4658×10^{-5}	2.4658×10^{-5}	6.668×10^{-22}	-
α_b [END]	-1.0462×10^{-4}	-1.0462×10^{-4}	3.689×10^{-22}	-
η_a [END]	3.2967×10^{-2}	3.2967×10^{-2}	8.517×10^{-23}	-
η'_a [END]	-3.7558×10^{-7}	-3.7558×10^{-7}	3.522×10^{-23}	-
R_{56} [END]	1.2809×10^{-1}	2.6117×10^{-1}	1.771×10^{13}	-
$\max(\beta_a)$	7.0000×10^2	3.0368×10^2	0	M13Q12
$\max(\beta_b)$	7.0000×10^2	1.7258×10^2	0	M13Q9
Fourth Pass				
β_a [END]	1.5386×10^0	1.5386×10^0	1.333×10^{-18}	-
β_b [END]	1.1607×10^1	1.1607×10^1	6.109×10^{-17}	-
α_a [END]	2.4713×10^{-5}	2.4713×10^{-5}	1.503×10^{-22}	-

Continued on next page

Table 8: (Continued)

Parameter	Target/Limit	Model Value	Merit	Location
α_b [END]	-1.1455×10^{-4}	-1.1455×10^{-4}	2.483×10^{-26}	-
η_a [END]	4.8495×10^{-2}	4.8495×10^{-2}	2.644×10^{-21}	-
η'_a [END]	-5.3096×10^{-7}	-5.3096×10^{-7}	1.567×10^{-23}	-
R_{56} [END]	1.9190×10^{-1}	1.9246×10^{-1}	3.144×10^8	-
$\max(\beta_a)$	7.0000×10^2	7.0000×10^2	0	D1506#5
$\max(\beta_b)$	7.0000×10^2	2.2086×10^2	0	D1505#8
Fifth Pass				
β_a [END]	1.6261×10^0	1.6261×10^0	4.450×10^{-18}	-
β_b [END]	1.4063×10^1	1.4063×10^1	1.392×10^{-17}	-
α_a [END]	2.5401×10^{-5}	2.5401×10^{-5}	2.412×10^{-21}	-
α_b [END]	-1.3987×10^{-4}	-1.3987×10^{-4}	1.722×10^{-23}	-
η_a [END]	6.1641×10^{-2}	6.1641×10^{-2}	1.282×10^{-20}	-
η'_a [END]	-6.6020×10^{-7}	-6.6020×10^{-7}	4.329×10^{-23}	-
R_{56} [END]	2.4233×10^{-1}	2.8420×10^{-1}	1.753×10^{12}	-
$\max(\beta_a)$	7.0000×10^2	1.9860×10^2	0	M17Q7
$\max(\beta_b)$	7.0000×10^2	7.0000×10^2	0	M17Q6
Sixth Pass				
β_a [END]	1.6824×10^0	1.6824×10^0	1.546×10^{-18}	-
β_b [END]	2.2819×10^1	2.2819×10^1	4.089×10^{-17}	-
α_a [END]	2.6113×10^{-5}	2.6113×10^{-5}	4.884×10^{-23}	-
α_b [END]	-2.2893×10^{-4}	-2.2893×10^{-4}	1.541×10^{-23}	-
η_a [END]	7.2865×10^{-2}	7.2865×10^{-2}	1.454×10^{-20}	-
η'_a [END]	-7.6926×10^{-7}	-7.6926×10^{-7}	1.388×10^{-22}	-
R_{56} [END]	2.8081×10^{-1}	2.8375×10^{-1}	8.646×10^9	-
$\max(\beta_a)$	7.0000×10^2	1.6566×10^2	0	M19Q2
$\max(\beta_b)$	7.0000×10^2	1.3377×10^2	0	M19Q4

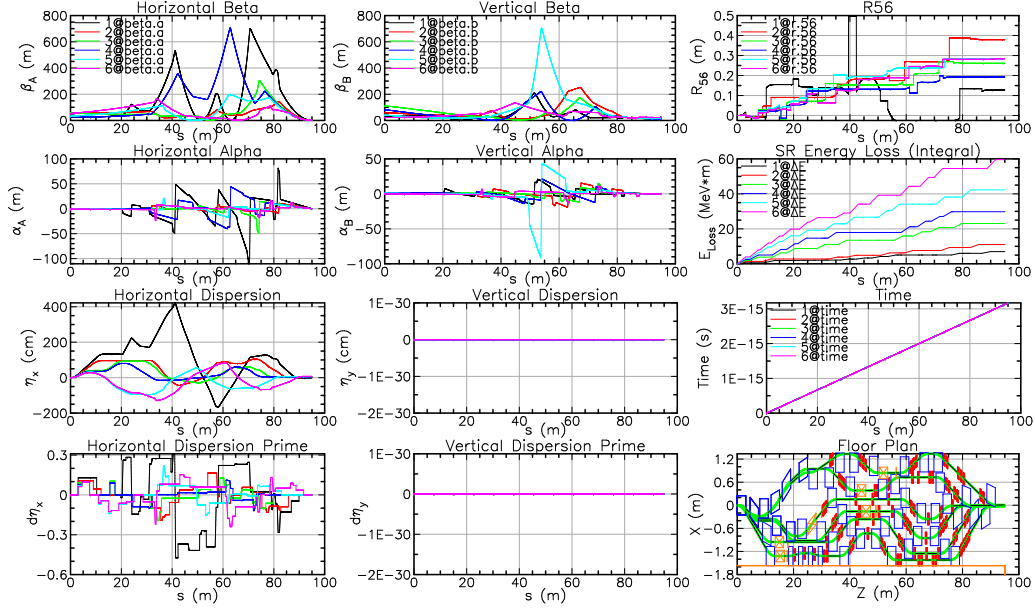


Figure 10: Matching solution from the SFT LINAC input into the BDC FFA match point. In this case, all of the Twiss parameters are always matched perfectly, and R_{56} compensation is ignored.

Table 9: Optimized integrated quadrupole strengths (K_1) for each of the six passes. The longitudinal position of the center of each magnet is given by the S-coordinate. All quadrupole strengths were limited to a range of $\pm 0.6 \text{ m}^{-2}$ during the optimization.

Element	S-Pos. (m)	K_1 (m^{-2})	Element	S-Pos. (m)	K_1 (m^{-2})
First Pass (P9) Quadrupoles					
M9Q1	20.66	-0.6000	M9Q11	57.28	0.5311
M9Q2	24.16	0.5405	M9Q12	58.28	0.5315
M9Q3	27.66	-0.1765	M9Q13	64.78	0.1258
M9Q4	31.16	-0.4388	M9Q14	65.78	-0.5395
M9Q5	32.16	-0.0596	M9Q15	69.78	-0.0459
M9Q6	40.36	-0.0969	M9Q16	70.78	0.5483
M9Q7	41.36	0.5243	M9Q17	79.88	-0.2963
M9Q8	46.66	0.0667	M9Q18	80.78	0.2021
M9Q9	51.66	-0.4195	M9Q19	81.68	0.6000
M9Q10	52.66	-0.0911	M9Q20	82.58	-0.5658

Table 9: (Continued)

Element	S-Pos. (m)	K_1 (m^{-2})	Element	S-Pos. (m)	K_1 (m^{-2})
Second Pass (P11) Quadrupoles					
M11Q1	32.11	0.2937	M11Q8	63.28	-0.2033
M11Q2	36.36	-0.2157	M11Q9	67.54	-0.2161
M11Q3	37.36	-0.2807	M11Q10	71.80	0.1064
M11Q4	42.86	0.6000	M11Q11	77.21	0.1190
M11Q5	48.50	0.2439	M11Q12	78.21	-0.2094
M11Q6	57.86	0.5904	M11Q13	81.21	-0.0447
M11Q7	58.86	-0.1868	M11Q14	82.21	0.3856
Third Pass (P13) Quadrupoles					
M13Q1	34.16	0.5247	M13Q7	60.66	0.6000
M13Q2	35.16	-0.6000	M13Q8	61.66	-0.1637
M13Q3	43.66	0.0405	M13Q9	67.28	-0.3358
M13Q4	50.55	0.6000	M13Q10	72.46	-0.0471
M13Q5	55.30	-0.4086	M13Q11	73.46	-0.2897
M13Q6	59.66	0.0059	M13Q12	74.46	0.6000
Fourth Pass (P15) Quadrupoles					
M15Q1	30.86	0.1734	M15Q6	62.04	0.0240
M15Q2	31.66	-0.6000	M15Q7	63.04	0.3249
M15Q3	42.35	0.3072	M15Q8	68.11	-0.0233
M15Q4	48.36	-0.1554	M15Q9	72.70	-0.6000
M15Q5	54.05	-0.3893	M15Q10	76.62	0.3266
Fifth Pass (P17) Quadrupoles					
M17Q1	36.56	0.6000	M17Q8	64.50	0.0142
M17Q2	37.36	-0.4601	M17Q9	68.63	-0.0002
M17Q3	38.16	0.0734	M17Q10	69.63	-0.0652
M17Q4	49.23	0.1396	M17Q11	74.48	-0.0613
M17Q5	49.87	0.6000	M17Q12	75.48	0.0164
M17Q6	54.09	-0.5447	M17Q13	77.48	0.0232
M17Q7	62.50	0.2968	M17Q14	78.48	0.1903
Sixth Pass (P19) Quadrupoles					

Table 9: (Continued)

Element	S-Pos. (m)	K_1 (m^{-2})	Element	S-Pos. (m)	K_1 (m^{-2})
M19Q1	33.36	-0.4061	M19Q9	73.75	-0.5500
M19Q2	33.96	0.5500	M19Q10	74.75	0.5479
M19Q3	43.86	0.0054	M19Q11	78.75	0.5500
M19Q4	44.86	-0.1742	M19Q12	79.75	-0.5500
M19Q5	45.86	-0.0168	M19Q13	80.75	0.1361
M19Q6	61.81	0.5877	M19Q14	86.75	0.5500
M19Q7	62.81	0.2850	M19Q15	87.75	-0.4598
M19Q8	63.81	-0.5652			

A.1.2. Weakly Focusing Triplet LINAC Input

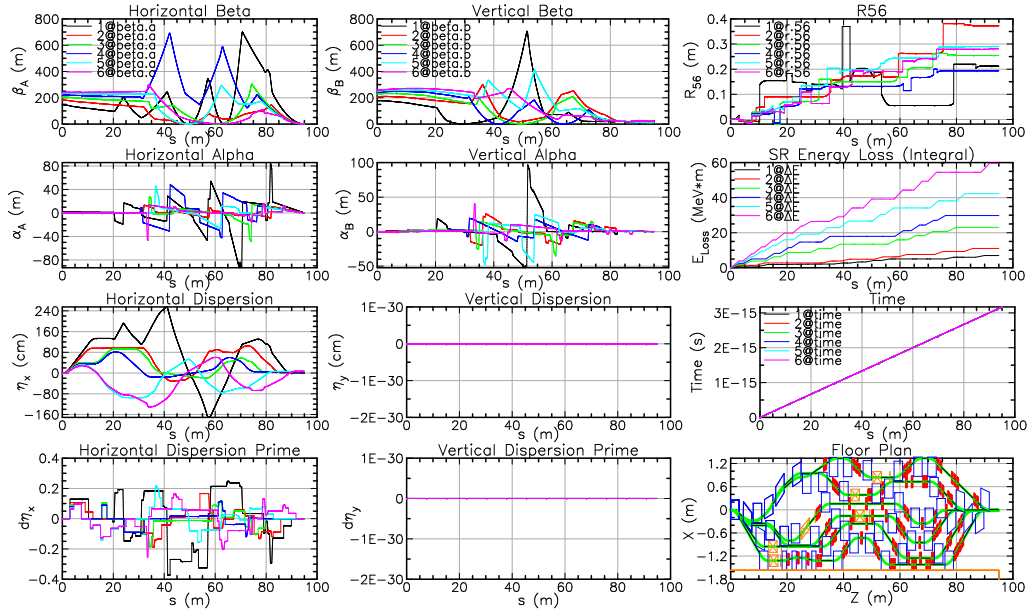


Figure 11: Matching solution from the WFT LINAC input into the BDC FFA match point. In this case, all of the Twiss parameters are always matched perfectly, and R_{56} compensation is ignored.

Table 10: Complete summary of Twiss parameter optimization constraints for the matching case of the WFT LINAC input and the BDC match point in the FFA Arc, excluding R_{56} matching. This includes target values for optical functions at the beamline end-point and maximum value limits throughout the line for each of the six energy passes.

Parameter	Target/Limit	Model Value	Merit	Location
First Pass				
β_a [END]	6.6586×10^{-1}	6.6586×10^{-1}	3.462×10^{-19}	-
β_b [END]	1.2039×10^1	1.2039×10^1	1.262×10^{-19}	-
α_a [END]	4.3124×10^{-5}	4.3124×10^{-5}	1.149×10^{-20}	-
α_b [END]	-1.1741×10^{-4}	-1.1741×10^{-4}	5.772×10^{-24}	-
η_a [END]	-7.8352×10^{-3}	-7.8352×10^{-3}	6.415×10^{-24}	-
η'_a [END]	4.3951×10^{-8}	4.3951×10^{-8}	2.939×10^{-23}	-
R_{56} [END]	-7.0886×10^{-2}	2.1209×10^{-1}	8.008×10^{13}	-
$\max(\beta_a)$	7.0000×10^2	7.0000×10^2	0	M9Q16
$\max(\beta_b)$	7.0000×10^2	7.0000×10^2	0	D908#2
Second Pass				
β_a [END]	1.1641×10^0	1.1641×10^0	2.174×10^{-19}	-
β_b [END]	1.0662×10^1	1.0662×10^1	0	-
α_a [END]	2.6829×10^{-5}	2.6829×10^{-5}	8.040×10^{-26}	-
α_b [END]	-1.0407×10^{-4}	-1.0407×10^{-4}	1.358×10^{-28}	-
η_a [END]	1.4456×10^{-2}	1.4456×10^{-2}	2.113×10^{-23}	-
η'_a [END]	-1.8690×10^{-7}	-1.8690×10^{-7}	4.234×10^{-25}	-
R_{56} [END]	4.4694×10^{-2}	3.7272×10^{-1}	1.076×10^{14}	-
$\max(\beta_a)$	7.0000×10^2	1.8362×10^2	0	BEGINNING
$\max(\beta_b)$	7.0000×10^2	2.9570×10^2	0	D1102#2
Third Pass				
β_a [END]	1.3998×10^0	1.3998×10^0	5.966×10^{-20}	-
β_b [END]	1.0669×10^1	1.0669×10^1	1.546×10^{-18}	-
α_a [END]	2.4658×10^{-5}	2.4658×10^{-5}	6.756×10^{-25}	-
α_b [END]	-1.0462×10^{-4}	-1.0462×10^{-4}	1.343×10^{-23}	-
η_a [END]	3.2967×10^{-2}	3.2967×10^{-2}	4.333×10^{-26}	-
η'_a [END]	-3.7558×10^{-7}	-3.7558×10^{-7}	2.938×10^{-26}	-
R_{56} [END]	1.2809×10^{-1}	2.5442×10^{-1}	1.596×10^{13}	-
$\max(\beta_a)$	7.0000×10^2	3.0368×10^2	0	M13Q12
$\max(\beta_b)$	7.0000×10^2	2.3230×10^2	0	MCB1

Continued on next page

Table 10: (Continued)

Parameter	Target/Limit	Model Value	Merit	Location
Fourth Pass				
β_a [END]	1.5386×10^0	1.5386×10^0	4.437×10^{-19}	-
β_b [END]	1.1607×10^1	1.1607×10^1	1.262×10^{-17}	-
α_a [END]	2.4713×10^{-5}	2.4713×10^{-5}	1.011×10^{-21}	-
α_b [END]	-1.1455×10^{-4}	-1.1455×10^{-4}	2.577×10^{-22}	-
η_a [END]	4.8495×10^{-2}	4.8495×10^{-2}	2.123×10^{-24}	-
η'_a [END]	-5.3096×10^{-7}	-5.3096×10^{-7}	1.637×10^{-28}	-
R_{56} [END]	1.9190×10^{-1}	1.9366×10^{-1}	3.085×10^9	-
$\max(\beta_a)$	7.0000×10^2	6.8792×10^2	0	D1505#2
$\max(\beta_b)$	7.0000×10^2	2.4895×10^2	0	MCB2
Fifth Pass				
β_a [END]	1.6261×10^0	1.6261×10^0	7.499×10^{-19}	-
β_b [END]	1.4063×10^1	1.4063×10^1	3.818×10^{-18}	-
α_a [END]	2.5401×10^{-5}	2.5401×10^{-5}	2.474×10^{-22}	-
α_b [END]	-1.3987×10^{-4}	-1.3987×10^{-4}	3.005×10^{-23}	-
η_a [END]	6.1641×10^{-2}	6.1641×10^{-2}	2.123×10^{-24}	-
η'_a [END]	-6.6020×10^{-7}	-6.6020×10^{-7}	1.595×10^{-26}	-
R_{56} [END]	2.4233×10^{-1}	2.8971×10^{-1}	2.245×10^{12}	-
$\max(\beta_a)$	7.0000×10^2	2.9238×10^2	0	M17Q7
$\max(\beta_b)$	7.0000×10^2	4.0781×10^2	0	M17Q6
Sixth Pass				
β_a [END]	1.6824×10^0	1.6824×10^0	2.848×10^{-18}	-
β_b [END]	2.2819×10^1	2.2819×10^1	4.544×10^{-18}	-
α_a [END]	2.6113×10^{-5}	2.6113×10^{-5}	5.525×10^{-23}	-
α_b [END]	-2.2893×10^{-4}	-2.2893×10^{-4}	1.274×10^{-23}	-
η_a [END]	7.2865×10^{-2}	7.2865×10^{-2}	4.391×10^{-22}	-
η'_a [END]	-7.6926×10^{-7}	-7.6926×10^{-7}	7.236×10^{-24}	-
R_{56} [END]	2.8081×10^{-1}	2.8153×10^{-1}	5.159×10^8	-
$\max(\beta_a)$	7.0000×10^2	2.9888×10^2	0	M19Q2
$\max(\beta_b)$	7.0000×10^2	2.7170×10^2	0	MCB4B

Table 11: Optimized integrated quadrupole strengths (K_1) for each of the six passes. The longitudinal position of the center of each magnet is given by the S-coordinate. All quadrupole strengths were limited to a range of $\pm 0.6 \text{ m}^{-2}$ during the optimization.

Element	S-Pos. (m)	K_1 (m^{-2})	Element	S-Pos. (m)	K_1 (m^{-2})
First Pass (P9) Quadrupoles					
M9Q1	20.66	-0.4107	M9Q11	57.28	0.5916
M9Q2	24.16	0.4979	M9Q12	58.28	0.3052
M9Q3	27.66	-0.0627	M9Q13	64.78	0.3239
M9Q4	31.16	-0.6000	M9Q14	65.78	-0.6000
M9Q5	32.16	-0.1398	M9Q15	69.78	0.0797
M9Q6	40.36	0.0112	M9Q16	70.78	0.4543
M9Q7	41.36	0.4937	M9Q17	79.88	-0.1930
M9Q8	46.66	0.0444	M9Q18	80.78	0.2105
M9Q9	51.66	-0.5985	M9Q19	81.68	0.5356
M9Q10	52.66	0.1025	M9Q20	82.58	-0.6000
Second Pass (P11) Quadrupoles					
M11Q1	32.11	0.2819	M11Q8	63.28	-0.1974
M11Q2	36.36	-0.3954	M11Q9	67.54	-0.2161
M11Q3	37.36	-0.0597	M11Q10	71.80	0.1064
M11Q4	42.86	0.4588	M11Q11	77.21	0.1190
M11Q5	48.50	0.5436	M11Q12	78.21	-0.2094
M11Q6	57.86	0.6000	M11Q13	81.21	-0.0447
M11Q7	58.86	-0.1919	M11Q14	82.21	0.3856
Third Pass (P13) Quadrupoles					
M13Q1	34.16	0.4772	M13Q7	60.66	0.4468
M13Q2	35.16	-0.6000	M13Q8	61.66	-0.6000
M13Q3	43.66	0.1954	M13Q9	67.28	-0.2555
M13Q4	50.55	0.0150	M13Q10	72.46	0.0224
M13Q5	55.30	-0.0578	M13Q11	73.46	-0.2882
M13Q6	59.66	0.3134	M13Q12	74.46	0.6000
Fourth Pass (P15) Quadrupoles					
M15Q1	30.86	0.1306	M15Q6	62.04	-0.0548
M15Q2	31.66	-0.3726	M15Q7	63.04	0.3687

Table 11: (Continued)

Element	S-Pos. (m)	K_1 (m ⁻²)	Element	S-Pos. (m)	K_1 (m ⁻²)
M15Q3	42.35	0.3236	M15Q8	68.11	-0.0075
M15Q4	48.36	-0.2390	M15Q9	72.70	-0.6000
M15Q5	54.05	-0.4206	M15Q10	76.62	0.3420
Fifth Pass (P17) Quadrupoles					
M17Q1	36.56	0.6000	M17Q8	64.50	0.0091
M17Q2	37.36	-0.1334	M17Q9	68.63	-0.0419
M17Q3	38.16	-0.4361	M17Q10	69.63	-0.1255
M17Q4	49.23	0.1614	M17Q11	74.48	-0.0613
M17Q5	49.87	0.5989	M17Q12	75.48	0.0164
M17Q6	54.09	-0.4792	M17Q13	77.48	0.0232
M17Q7	62.50	0.3699	M17Q14	78.48	0.1903
Sixth Pass (P19) Quadrupoles					
M19Q1	33.36	-0.4819	M19Q9	73.75	-0.4768
M19Q2	33.96	0.5784	M19Q10	74.75	0.4529
M19Q3	43.86	0.1211	M19Q11	78.75	0.5500
M19Q4	44.86	-0.1310	M19Q12	79.75	-0.5500
M19Q5	45.86	-0.1182	M19Q13	80.75	0.1361
M19Q6	61.81	0.6000	M19Q14	86.75	0.5500
M19Q7	62.81	0.3919	M19Q15	87.75	-0.4598
M19Q8	63.81	-0.5783			

A.2. Matches Including R_{56} Compensation

The following will show match solutions, including R_{56} compensation. They are broken apart by input LINAC optics; either from the SFT or WFT.

A.2.1. Strong Focusing Triplet LINAC Input

There are two matches which use the SFT as inputs: one from SFT into the Beginning match point in the FFA Cell, and another from SFT to the BDC match point in the FFA Cell. Both are shown below, and the reader is requested to take care when reading the following tables.

Showing first the SFT matching into the Beginning FFA Cell match point:

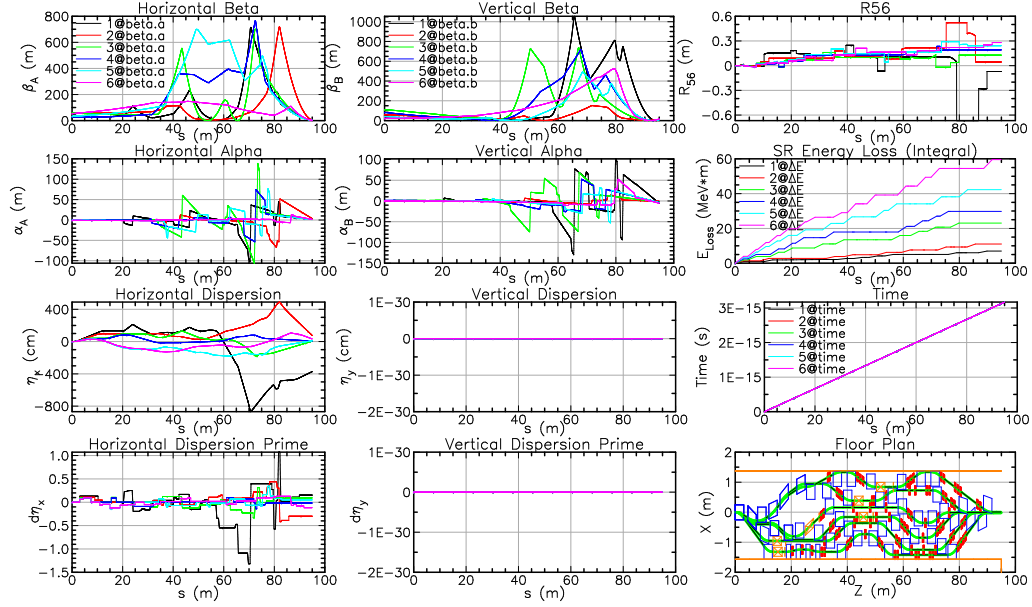


Figure 12: Matching solution from the SFT LINAC input into the Beginning FFA match point. In this case, R_{56} and $\beta_{x,y}$ is always matched perfectly, while $\alpha_{x,y}$ and η_a and η'_a have matches of varying strength.

Table 12: Complete summary of Twiss parameter optimization constraints for the matching case of the SFT LINAC input and the Beginning match point in the FFA Arc, including R_{56} matching. This includes target values for optical functions at the beamline end-point and maximum value limits throughout the line for each of the six energy passes.

Parameter	Target/Limit	Model Value	Merit	Location
First Pass				
β_a [END]	4.1573×10^0	4.1573×10^0	1.138×10^1	-
β_b [END]	6.5151×10^0	6.5151×10^0	7.290×10^0	-
α_a [END]	3.0489×10^0	1.2360×10^0	3.286×10^6	-
α_b [END]	-3.1896×10^0	-6.0894×10^0	8.409×10^6	-
η_a [END]	2.7200×10^{-2}	-3.7165×10^0	1.402×10^9	-
η'_a [END]	-1.9800×10^{-2}	1.5193×10^{-1}	2.949×10^6	-
R_{56} [END]	-7.0886×10^{-2}	-7.0886×10^{-2}	1.308×10^{-13}	-
$\max(\beta_a)$	7.0000×10^2	7.1127×10^2	1.269×10^2	M9Q16
$\max(\beta_b)$	7.0000×10^2	1.0447×10^3	1.188×10^5	M9Q14

Continued on next page

Table 12: (Continued)

Parameter	Target/Limit	Model Value	Merit	Location
Second Pass				
β_a [END]	2.9506×10^0	2.9506×10^0	1.596×10^1	-
β_b [END]	6.4768×10^0	6.4768×10^0	5.170×10^0	-
α_a [END]	1.8215×10^0	3.1861×10^0	1.862×10^6	-
α_b [END]	-3.0366×10^0	-7.1030×10^{-1}	5.412×10^6	-
η_a [END]	4.5700×10^{-2}	7.4439×10^{-1}	4.882×10^7	-
η'_a [END]	-2.6400×10^{-2}	-3.0046×10^{-1}	7.511×10^6	-
R_{56} [END]	4.4694×10^{-2}	4.4694×10^{-2}	1.531×10^{-13}	-
$\max(\beta_a)$	7.0000×10^2	7.1015×10^2	1.031×10^2	M11Q14
$\max(\beta_b)$	7.0000×10^2	1.5171×10^2	0	M11Q10
Third Pass				
β_a [END]	2.7180×10^0	2.7180×10^0	1.330×10^1	-
β_b [END]	6.9948×10^0	6.9948×10^0	1.427×10^1	-
α_a [END]	1.5388×10^0	1.1993×10^0	1.152×10^5	-
α_b [END]	-3.2063×10^0	-2.2045×10^0	1.004×10^6	-
η_a [END]	6.0800×10^{-2}	4.8292×10^{-2}	1.564×10^4	-
η'_a [END]	-3.0900×10^{-2}	9.3643×10^{-2}	1.551×10^6	-
R_{56} [END]	1.2809×10^{-1}	1.2809×10^{-1}	1.926×10^{-17}	-
$\max(\beta_a)$	7.0000×10^2	7.0047×10^2	2.218×10^{-1}	M13Q10
$\max(\beta_b)$	7.0000×10^2	7.2508×10^2	6.292×10^2	M13Q4
Fourth Pass				
β_a [END]	2.6023×10^0	2.6023×10^0	1.485×10^1	-
β_b [END]	8.0350×10^0	8.0350×10^0	2.944×10^0	-
α_a [END]	1.3995×10^0	9.8180×10^{-1}	1.745×10^5	-
α_b [END]	-3.6359×10^0	-3.5727×10^0	4.000×10^3	-
η_a [END]	7.3500×10^{-2}	7.4246×10^{-2}	5.566×10^1	-
η'_a [END]	-3.3600×10^{-2}	-1.6806×10^{-2}	2.820×10^4	-
R_{56} [END]	1.9190×10^{-1}	1.9190×10^{-1}	1.926×10^{-17}	-
$\max(\beta_a)$	7.0000×10^2	7.5858×10^2	3.432×10^3	D1508#2
$\max(\beta_b)$	7.0000×10^2	7.1406×10^2	1.978×10^2	D1507#2
Fifth Pass				
β_a [END]	2.5213×10^0	2.5213×10^0	1.257×10^1	-

Continued on next page

Table 12: (Continued)

Parameter	Target/Limit	Model Value	Merit	Location
β_b [END]	1.0132×10^1	1.0132×10^1	5.861×10^0	-
α_a [END]	1.3111×10^0	8.9904×10^{-1}	1.698×10^5	-
α_b [END]	-4.5492×10^0	-4.2207×10^0	1.079×10^5	-
η_a [END]	8.4100×10^{-2}	1.0620×10^{-1}	4.883×10^4	-
η'_a [END]	-3.4900×10^{-2}	5.0860×10^{-2}	7.355×10^5	-
R_{56} [END]	2.4233×10^{-1}	2.4233×10^{-1}	2.496×10^{-16}	-
$\max(\beta_a)$	7.0000×10^2	7.0030×10^2	8.964×10^{-2}	M17Q4
$\max(\beta_b)$	7.0000×10^2	4.8923×10^2	0	M17Q9
Sixth Pass				
β_a [END]	2.4552×10^0	2.4552×10^0	4.437×10^{-19}	-
β_b [END]	1.6840×10^1	1.6840×10^1	2.840×10^{-17}	-
α_a [END]	1.2471×10^0	1.3639×10^0	1.365×10^4	-
α_b [END]	-7.5245×10^0	-5.3041×10^0	4.930×10^6	-
η_a [END]	9.3200×10^{-2}	3.3108×10^{-1}	5.659×10^6	-
η'_a [END]	-3.5000×10^{-2}	-1.1699×10^{-1}	6.723×10^5	-
R_{56} [END]	2.8081×10^{-1}	2.8081×10^{-1}	5.208×10^{-16}	-
$\max(\beta_a)$	7.0000×10^2	1.4796×10^2	0	M19Q5
$\max(\beta_b)$	7.0000×10^2	5.2637×10^2	0	D1912#11

Table 13: Optimized integrated quadrupole strengths (K_1) for each of the six passes. The longitudinal position of the center of each magnet is given by the S-coordinate. All quadrupole strengths were limited to a range of $\pm 0.6 \text{ m}^{-2}$ during the optimization.

Element	S-Pos. (m)	K_1 (m^{-2})	Element	S-Pos. (m)	K_1 (m^{-2})
First Pass (P9) Quadrupoles					
M9Q1	20.66	-0.5323	M9Q11	57.28	0.4988
M9Q2	24.16	0.5935	M9Q12	58.28	0.4633
M9Q3	27.66	-0.0619	M9Q13	64.78	0.0642
M9Q4	31.16	-0.3722	M9Q14	65.78	-0.5706
M9Q5	32.16	-0.2316	M9Q15	69.78	-0.1051
M9Q6	40.36	-0.4595	M9Q16	70.78	0.5469
M9Q7	41.36	0.1046	M9Q17	79.88	-0.4392
M9Q8	46.66	0.5083	M9Q18	80.78	0.2952

Table 13: (Continued)

Element	S-Pos. (m)	K_1 (m^{-2})	Element	S-Pos. (m)	K_1 (m^{-2})
M9Q9	51.66	-0.1289	M9Q19	81.68	0.5041
M9Q10	52.66	-0.0512	M9Q20	82.58	-0.5999
Second Pass (P11) Quadrupoles					
M11Q1	32.11	-0.0790	M11Q8	63.28	-0.0599
M11Q2	36.36	-0.2096	M11Q9	67.54	0.0295
M11Q3	37.36	0.2669	M11Q10	71.80	-0.1801
M11Q4	42.86	0.3198	M11Q11	77.21	-0.2314
M11Q5	48.50	-0.6000	M11Q12	78.21	-0.1088
M11Q6	57.86	-0.0739	M11Q13	81.21	0.0944
M11Q7	58.86	-0.0665	M11Q14	82.21	0.4155
Third Pass (P13) Quadrupoles					
M13Q1	34.16	-0.5596	M13Q7	60.66	0.3326
M13Q2	35.16	-0.1211	M13Q8	61.66	0.6000
M13Q3	43.66	0.5268	M13Q9	67.28	-0.5479
M13Q4	50.55	-0.3757	M13Q10	72.46	0.4494
M13Q5	55.30	-0.1940	M13Q11	73.46	0.5829
M13Q6	59.66	0.2639	M13Q12	74.46	-0.6000
Fourth Pass (P15) Quadrupoles					
M15Q1	30.86	0.1741	M15Q6	62.04	0.0987
M15Q2	31.66	-0.5962	M15Q7	63.04	-0.0284
M15Q3	42.35	0.2561	M15Q8	68.11	-0.3036
M15Q4	48.36	0.0415	M15Q9	72.70	0.4761
M15Q5	54.05	-0.1118	M15Q10	76.62	-0.2987
Fifth Pass (P17) Quadrupoles					
M17Q1	36.56	-0.1813	M17Q8	64.50	-0.0004
M17Q2	37.36	-0.6000	M17Q9	68.63	-0.2730
M17Q3	38.16	0.4435	M17Q10	69.63	-0.0258
M17Q4	49.23	0.1266	M17Q11	74.48	-0.1663
M17Q5	49.87	0.0484	M17Q12	75.48	0.4173
M17Q6	54.09	-0.0690	M17Q13	77.48	0.3817

Table 13: (Continued)

Element	S-Pos. (m)	K_1 (m^{-2})	Element	S-Pos. (m)	K_1 (m^{-2})
M17Q7	62.50	0.1435	M17Q14	78.48	-0.6000
Sixth Pass (P19) Quadrupoles					
M19Q1	33.36	0.0703	M19Q9	73.75	-0.0569
M19Q2	33.96	-0.0348	M19Q10	74.75	0.0583
M19Q3	43.86	-0.0335	M19Q11	78.75	-0.0235
M19Q4	44.86	0.0024	M19Q12	79.75	-0.1932
M19Q5	45.86	0.0542	M19Q13	80.75	-0.1504
M19Q6	61.81	0.0730	M19Q14	86.75	0.5230
M19Q7	62.81	0.0047	M19Q15	87.75	-0.0678
M19Q8	63.81	-0.0322			

Showing next the SFT matching into the BDC FFA Cell match point:

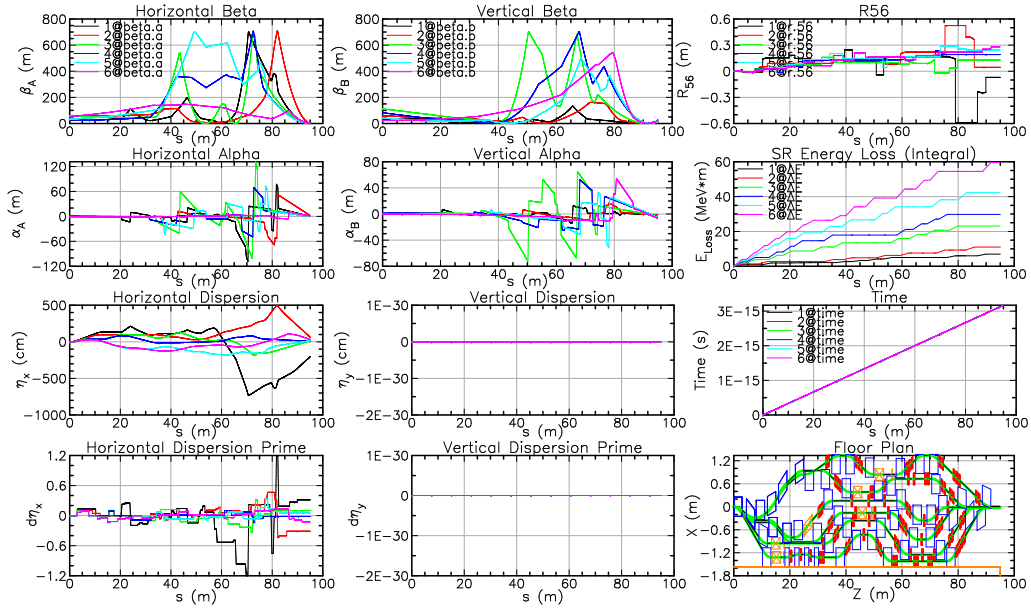


Figure 13: Matching solution from the SFT LINAC input into the BDC FFA match point. In this case, R_{56} and $\beta_{x,y}$ is always matched perfectly, while $\alpha_{x,y}$ and η_a and η'_a have matches of varying strength.

Table 14: Complete summary of Twiss parameter optimization constraints for the matching case of the SFT LINAC input and the BDC match point in the FFA Arc, including R_{56} matching. This includes target values for optical functions at the beamline end-point and maximum value limits throughout the line for each of the six energy passes.

Parameter	Target/Limit	Model Value	Merit	Location
First Pass				
β_a [END]	6.6586×10^{-1}	6.6586×10^{-1}	2.381×10^{-18}	-
β_b [END]	1.2039×10^1	1.2039×10^1	2.788×10^{-16}	-
α_a [END]	4.3124×10^{-5}	-4.2697×10^{-2}	1.827×10^3	-
α_b [END]	-1.1741×10^{-4}	-1.1382×10^0	1.295×10^6	-
η_a [END]	-7.8352×10^{-3}	-2.0235×10^0	4.063×10^8	-
η'_a [END]	4.3951×10^{-8}	3.1545×10^{-1}	9.951×10^6	-
R_{56} [END]	-7.0886×10^{-2}	-7.0886×10^{-2}	5.268×10^{-14}	-
$\max(\beta_a)$	7.0000×10^2	7.0000×10^2	0	M9Q16
$\max(\beta_b)$	7.0000×10^2	1.3102×10^2	0	M9Q14
Second Pass				
β_a [END]	1.1641×10^0	1.1641×10^0	8.332×10^{-20}	-
β_b [END]	1.0662×10^1	1.0662×10^1	1.136×10^{-16}	-
α_a [END]	2.6829×10^{-5}	1.8910×10^0	3.576×10^6	-
α_b [END]	-1.0407×10^{-4}	-1.6655×10^0	2.773×10^6	-
η_a [END]	1.4456×10^{-2}	6.3057×10^{-1}	3.796×10^7	-
η'_a [END]	-1.8690×10^{-7}	-3.1314×10^{-1}	9.806×10^6	-
R_{56} [END]	4.4694×10^{-2}	4.4694×10^{-2}	1.628×10^{-13}	-
$\max(\beta_a)$	7.0000×10^2	7.0000×10^2	0	M11Q14
$\max(\beta_b)$	7.0000×10^2	1.6213×10^2	0	M11Q10
Third Pass				
β_a [END]	1.3998×10^0	1.3998×10^0	1.804×10^{-15}	-
β_b [END]	1.0669×10^1	1.0669×10^1	2.300×10^{-17}	-
α_a [END]	2.4658×10^{-5}	5.5600×10^{-1}	3.091×10^5	-
α_b [END]	-1.0462×10^{-4}	-2.6784×10^0	7.173×10^6	-
η_a [END]	3.2967×10^{-2}	1.2496×10^{-1}	8.463×10^5	-
η'_a [END]	-3.7558×10^{-7}	9.9008×10^{-2}	9.803×10^5	-
R_{56} [END]	1.2809×10^{-1}	1.2809×10^{-1}	6.240×10^{-17}	-
$\max(\beta_a)$	7.0000×10^2	6.7114×10^2	0	D1308#5
$\max(\beta_b)$	7.0000×10^2	7.0000×10^2	0	M13Q4

Continued on next page

Table 14: (Continued)

Parameter	Target/Limit	Model Value	Merit	Location
Fourth Pass				
β_a [END]	1.5386×10^0	1.5386×10^0	4.378×10^{-17}	-
β_b [END]	1.1607×10^1	1.1607×10^1	2.908×10^{-16}	-
α_a [END]	2.4713×10^{-5}	3.8831×10^{-1}	1.508×10^5	-
α_b [END]	-1.1455×10^{-4}	-4.3379×10^0	1.882×10^7	-
η_a [END]	4.8495×10^{-2}	7.4420×10^{-2}	6.721×10^4	-
η'_a [END]	-5.3096×10^{-7}	-1.7070×10^{-2}	2.914×10^4	-
R_{56} [END]	1.9190×10^{-1}	1.9190×10^{-1}	1.233×10^{-17}	-
$\max(\beta_a)$	7.0000×10^2	7.0000×10^2	0	D1508#2
$\max(\beta_b)$	7.0000×10^2	7.0000×10^2	0	D1507#2
Fifth Pass				
β_a [END]	1.6261×10^0	1.6261×10^0	2.935×10^{-17}	-
β_b [END]	1.4063×10^1	1.4063×10^1	4.089×10^{-17}	-
α_a [END]	2.5401×10^{-5}	4.2785×10^{-1}	1.830×10^5	-
α_b [END]	-1.3987×10^{-4}	-5.0845×10^0	2.585×10^7	-
η_a [END]	6.1641×10^{-2}	1.4104×10^{-1}	6.304×10^5	-
η'_a [END]	-6.6020×10^{-7}	5.1050×10^{-2}	2.606×10^5	-
R_{56} [END]	2.4233×10^{-1}	2.4233×10^{-1}	3.775×10^{-17}	-
$\max(\beta_a)$	7.0000×10^2	7.0000×10^2	0	M17Q4
$\max(\beta_b)$	7.0000×10^2	4.9647×10^2	0	M17Q9
Sixth Pass				
β_a [END]	1.6824×10^0	1.6824×10^0	1.972×10^{-21}	-
β_b [END]	2.2819×10^1	2.2819×10^1	2.133×10^{-17}	-
α_a [END]	2.6113×10^{-5}	9.5193×10^{-1}	9.061×10^5	-
α_b [END]	-2.2893×10^{-4}	-6.5168×10^0	4.247×10^7	-
η_a [END]	7.2865×10^{-2}	3.1295×10^{-1}	5.764×10^6	-
η'_a [END]	-7.6926×10^{-7}	-1.2359×10^{-1}	1.528×10^6	-
R_{56} [END]	2.8081×10^{-1}	2.8081×10^{-1}	6.933×10^{-16}	-
$\max(\beta_a)$	7.0000×10^2	1.4796×10^2	0	M19Q5
$\max(\beta_b)$	7.0000×10^2	5.4139×10^2	0	D1912#11

Table 15: Optimized integrated quadrupole strengths (K_1) for each of the six passes. The longitudinal position of the center of each magnet is given by the S-coordinate. All quadrupole strengths were limited to a range of $\pm 0.6 \text{ m}^{-2}$ during the optimization.

Element	S-Pos. (m)	K_1 (m^{-2})	Element	S-Pos. (m)	K_1 (m^{-2})
First Pass (P9) Quadrupoles					
M9Q1	20.66	-0.5323	M9Q11	57.28	0.4988
M9Q2	24.16	0.5935	M9Q12	58.28	0.4633
M9Q3	27.66	-0.0619	M9Q13	64.78	0.0642
M9Q4	31.16	-0.3722	M9Q14	65.78	-0.5706
M9Q5	32.16	-0.2316	M9Q15	69.78	-0.1051
M9Q6	40.36	-0.4237	M9Q16	70.78	0.5469
M9Q7	41.36	0.1392	M9Q17	79.88	-0.4223
M9Q8	46.66	0.4987	M9Q18	80.78	0.3262
M9Q9	51.66	-0.3068	M9Q19	81.68	0.5520
M9Q10	52.66	-0.1841	M9Q20	82.58	-0.5336
Second Pass (P11) Quadrupoles					
M11Q1	32.11	-0.0790	M11Q8	63.28	-0.0599
M11Q2	36.36	-0.2096	M11Q9	67.54	0.0295
M11Q3	37.36	0.2669	M11Q10	71.80	-0.1801
M11Q4	42.86	0.3198	M11Q11	77.21	-0.2314
M11Q5	48.50	-0.6000	M11Q12	78.21	-0.1088
M11Q6	57.86	-0.0899	M11Q13	81.21	0.0944
M11Q7	58.86	-0.0918	M11Q14	82.21	0.4208
Third Pass (P13) Quadrupoles					
M13Q1	34.16	-0.5537	M13Q7	60.66	0.3299
M13Q2	35.16	-0.1167	M13Q8	61.66	0.6000
M13Q3	43.66	0.5254	M13Q9	67.28	-0.5533
M13Q4	50.55	-0.3758	M13Q10	72.46	0.4333
M13Q5	55.30	-0.1960	M13Q11	73.46	0.5880
M13Q6	59.66	0.2637	M13Q12	74.46	-0.5772
Fourth Pass (P15) Quadrupoles					
M15Q1	30.86	0.1741	M15Q6	62.04	0.1009
M15Q2	31.66	-0.6000	M15Q7	63.04	-0.0274

Table 15: (Continued)

Element	S-Pos. (m)	K_1 (m^{-2})	Element	S-Pos. (m)	K_1 (m^{-2})
M15Q3	42.35	0.1756	M15Q8	68.11	-0.3062
M15Q4	48.36	0.0529	M15Q9	72.70	0.4771
M15Q5	54.05	-0.1244	M15Q10	76.62	-0.2979
Fifth Pass (P17) Quadrupoles					
M17Q1	36.56	-0.1813	M17Q8	64.50	0.0018
M17Q2	37.36	-0.6000	M17Q9	68.63	-0.2765
M17Q3	38.16	0.4435	M17Q10	69.63	-0.0061
M17Q4	49.23	0.1266	M17Q11	74.48	-0.1674
M17Q5	49.87	0.0484	M17Q12	75.48	0.4178
M17Q6	54.09	-0.0690	M17Q13	77.48	0.3821
M17Q7	62.50	0.1478	M17Q14	78.48	-0.5999
Sixth Pass (P19) Quadrupoles					
M19Q1	33.36	0.0703	M19Q9	73.75	-0.0585
M19Q2	33.96	-0.0348	M19Q10	74.75	0.0570
M19Q3	43.86	-0.0335	M19Q11	78.75	-0.0251
M19Q4	44.86	0.0024	M19Q12	79.75	-0.1948
M19Q5	45.86	0.0542	M19Q13	80.75	-0.1513
M19Q6	61.81	0.0754	M19Q14	86.75	0.5286
M19Q7	62.81	0.0064	M19Q15	87.75	-0.0635
M19Q8	63.81	-0.0312			

A.2.2. Weakly Focusing Triplet LINAC Input

Table 16: Complete summary of Twiss parameter optimization constraints for the matching case of the WFT LINAC input and the BDC match point in the FFA Arc, including R_{56} matching. This includes target values for optical functions at the beamline end-point and maximum value limits throughout the line for each of the six energy passes.

Parameter	Target/Limit	Model Value	Merit	Location
First Pass				
β_a [END]	6.6586×10^{-1}	6.6586×10^{-1}	4.437×10^{-21}	-
β_b [END]	1.2039×10^1	1.2039×10^1	1.546×10^{-18}	-

Continued on next page

Table 16: (Continued)

Parameter	Target/Limit	Model Value	Merit	Location
α_a [END]	4.3124×10^{-5}	4.3124×10^{-5}	3.585×10^{-22}	-
α_b [END]	-1.1741×10^{-4}	-1.1741×10^{-4}	4.641×10^{-23}	-
η_a [END]	-7.8352×10^{-3}	-2.7903×10^{-3}	2.545×10^3	-
η'_a [END]	4.3951×10^{-8}	1.0875×10^{-1}	1.183×10^6	-
R_{56} [END]	-7.0886×10^{-2}	-7.0886×10^{-2}	1.733×10^{-18}	-
$\max(\beta_a)$	7.0000×10^2	7.0000×10^2	1.837×10^{-21}	M9B11
$\max(\beta_b)$	7.0000×10^2	1.7815×10^2	0	BEGINNING
Second Pass				
β_a [END]	1.1641×10^0	1.1641×10^0	1.008×10^{-17}	-
β_b [END]	1.0662×10^1	1.0662×10^1	2.300×10^{-17}	-
α_a [END]	2.6829×10^{-5}	2.6829×10^{-5}	2.228×10^{-24}	-
α_b [END]	-1.0407×10^{-4}	-1.0407×10^{-4}	1.351×10^{-23}	-
η_a [END]	1.4456×10^{-2}	5.0798×10^{-1}	2.436×10^7	-
η'_a [END]	-1.8690×10^{-7}	-4.8296×10^{-1}	2.333×10^7	-
R_{56} [END]	4.4694×10^{-2}	4.4694×10^{-2}	1.204×10^{-18}	-
$\max(\beta_a)$	7.0000×10^2	1.8362×10^2	0	BEGINNING
$\max(\beta_b)$	7.0000×10^2	5.9605×10^2	0	D1103#2
Third Pass				
β_a [END]	1.3998×10^0	1.3998×10^0	1.098×10^{-16}	-
β_b [END]	1.0669×10^1	1.0669×10^1	5.099×10^{-15}	-
α_a [END]	2.4658×10^{-5}	1.0789×10^0	1.164×10^6	-
α_b [END]	-1.0462×10^{-4}	-4.7091×10^{-1}	2.217×10^5	-
η_a [END]	3.2967×10^{-2}	5.0604×10^{-1}	2.238×10^7	-
η'_a [END]	-3.7558×10^{-7}	-2.2781×10^{-1}	5.190×10^6	-
R_{56} [END]	1.2809×10^{-1}	1.2809×10^{-1}	1.850×10^{-15}	-
$\max(\beta_a)$	7.0000×10^2	7.0000×10^2	3.158×10^{-17}	M13Q12
$\max(\beta_b)$	7.0000×10^2	2.3230×10^2	0	MCB1
Fourth Pass				
β_a [END]	1.5386×10^0	1.5386×10^0	3.333×10^{-19}	-
β_b [END]	1.1607×10^1	1.1607×10^1	1.262×10^{-19}	-
α_a [END]	2.4713×10^{-5}	2.4713×10^{-5}	2.500×10^{-22}	-
α_b [END]	-1.1455×10^{-4}	-1.1455×10^{-4}	6.285×10^{-24}	-

Continued on next page

Table 16: (Continued)

Parameter	Target/Limit	Model Value	Merit	Location
η_a [END]	4.8495×10^{-2}	1.1647×10^{-1}	4.620×10^5	-
η'_a [END]	-5.3096×10^{-7}	9.7679×10^{-4}	9.552×10^1	-
R_{56} [END]	1.9190×10^{-1}	1.9190×10^{-1}	7.704×10^{-19}	-
$\max(\beta_a)$	7.0000×10^2	6.9511×10^2	0	D1505#2
$\max(\beta_b)$	7.0000×10^2	2.4895×10^2	0	MCB2
Fifth Pass				
β_a [END]	1.6261×10^0	1.6261×10^0	3.865×10^{-19}	-
β_b [END]	1.4063×10^1	1.4063×10^1	1.818×10^{-17}	-
α_a [END]	2.5401×10^{-5}	2.5401×10^{-5}	4.689×10^{-23}	-
α_b [END]	-1.3987×10^{-4}	-1.3987×10^{-4}	2.454×10^{-23}	-
η_a [END]	6.1641×10^{-2}	6.9842×10^{-1}	4.055×10^7	-
η'_a [END]	-6.6020×10^{-7}	-1.6724×10^{-2}	2.797×10^4	-
R_{56} [END]	2.4233×10^{-1}	2.4233×10^{-1}	7.704×10^{-19}	-
$\max(\beta_a)$	7.0000×10^2	2.4720×10^2	0	D1710#5
$\max(\beta_b)$	7.0000×10^2	6.0681×10^2	0	M17Q6
Sixth Pass				
β_a [END]	1.6824×10^0	1.6824×10^0	3.155×10^{-20}	-
β_b [END]	2.2819×10^1	2.2819×10^1	1.262×10^{-17}	-
α_a [END]	2.6113×10^{-5}	2.6113×10^{-5}	7.736×10^{-24}	-
α_b [END]	-2.2893×10^{-4}	-2.2893×10^{-4}	1.156×10^{-22}	-
η_a [END]	7.2865×10^{-2}	6.3143×10^{-2}	9.452×10^3	-
η'_a [END]	-7.6926×10^{-7}	-6.2086×10^{-4}	3.845×10^1	-
R_{56} [END]	2.8081×10^{-1}	2.8081×10^{-1}	0	-
$\max(\beta_a)$	7.0000×10^2	2.9889×10^2	0	M19Q2
$\max(\beta_b)$	7.0000×10^2	2.7170×10^2	0	MCB4B

Table 17: Optimized integrated quadrupole strengths (K_1) for each of the six passes. The longitudinal position of the center of each magnet is given by the S-coordinate. All quadrupole strengths were limited to a range of $\pm 0.6 \text{ m}^{-2}$ during the optimization.

Element	S-Pos. (m)	K_1 (m^{-2})	Element	S-Pos. (m)	K_1 (m^{-2})
First Pass (P9) Quadrupoles					

Table 17: (Continued)

Element	S-Pos. (m)	K_1 (m^{-2})	Element	S-Pos. (m)	K_1 (m^{-2})
M9Q1	20.66	-0.4724	M9Q11	57.28	0.5236
M9Q2	24.16	0.6000	M9Q12	58.28	0.5403
M9Q3	27.66	-0.2600	M9Q13	64.78	-0.1129
M9Q4	31.16	-0.6000	M9Q14	65.78	-0.3928
M9Q5	32.16	-0.4271	M9Q15	69.78	-0.1660
M9Q6	40.36	-0.1253	M9Q16	70.78	0.5417
M9Q7	41.36	0.5453	M9Q17	79.88	0.2857
M9Q8	46.66	0.1583	M9Q18	80.78	0.2811
M9Q9	51.66	-0.6000	M9Q19	81.68	-0.1065
M9Q10	52.66	0.0714	M9Q20	82.58	-0.5491
Second Pass (P11) Quadrupoles					
M11Q1	32.11	0.1350	M11Q8	63.28	-0.0939
M11Q2	36.36	-0.0002	M11Q9	67.54	-0.0687
M11Q3	37.36	0.2417	M11Q10	71.80	-0.1106
M11Q4	42.86	-0.5269	M11Q11	77.21	-0.1655
M11Q5	48.50	0.6000	M11Q12	78.21	-0.1339
M11Q6	57.86	0.5963	M11Q13	81.21	-0.1222
M11Q7	58.86	-0.4928	M11Q14	82.21	0.6000
Third Pass (P13) Quadrupoles					
M13Q1	34.16	-0.3901	M13Q7	60.66	-0.0095
M13Q2	35.16	0.4097	M13Q8	61.66	-0.1809
M13Q3	43.66	0.1338	M13Q9	67.28	-0.3596
M13Q4	50.55	-0.0937	M13Q10	72.46	-0.5005
M13Q5	55.30	-0.6000	M13Q11	73.46	0.0706
M13Q6	59.66	-0.2304	M13Q12	74.46	0.6000
Fourth Pass (P15) Quadrupoles					
M15Q1	30.86	0.1283	M15Q6	62.04	-0.0503
M15Q2	31.66	-0.3726	M15Q7	63.04	0.3662
M15Q3	42.35	0.3261	M15Q8	68.11	-0.0253
M15Q4	48.36	-0.2382	M15Q9	72.70	-0.6000
M15Q5	54.05	-0.4196	M15Q10	76.62	0.3542

Table 17: (Continued)

Element	S-Pos. (m)	K_1 (m^{-2})	Element	S-Pos. (m)	K_1 (m^{-2})
Fifth Pass (P17) Quadrupoles					
M17Q1	36.56	0.2012	M17Q8	64.50	-0.0014
M17Q2	37.36	-0.0837	M17Q9	68.63	-0.1290
M17Q3	38.16	-0.0721	M17Q10	69.63	-0.1160
M17Q4	49.23	-0.0697	M17Q11	74.48	0.1427
M17Q5	49.87	0.4606	M17Q12	75.48	0.2015
M17Q6	54.09	-0.4186	M17Q13	77.48	0.0679
M17Q7	62.50	0.3701	M17Q14	78.48	-0.0709
Sixth Pass (P19) Quadrupoles					
M19Q1	33.36	-0.4822	M19Q9	73.75	-0.4762
M19Q2	33.96	0.5789	M19Q10	74.75	0.4508
M19Q3	43.86	0.1200	M19Q11	78.75	0.5477
M19Q4	44.86	-0.1308	M19Q12	79.75	-0.5497
M19Q5	45.86	-0.1168	M19Q13	80.75	0.1366
M19Q6	61.81	0.6000	M19Q14	86.75	0.5520
M19Q7	62.81	0.3871	M19Q15	87.75	-0.4565
M19Q8	63.81	-0.5773			

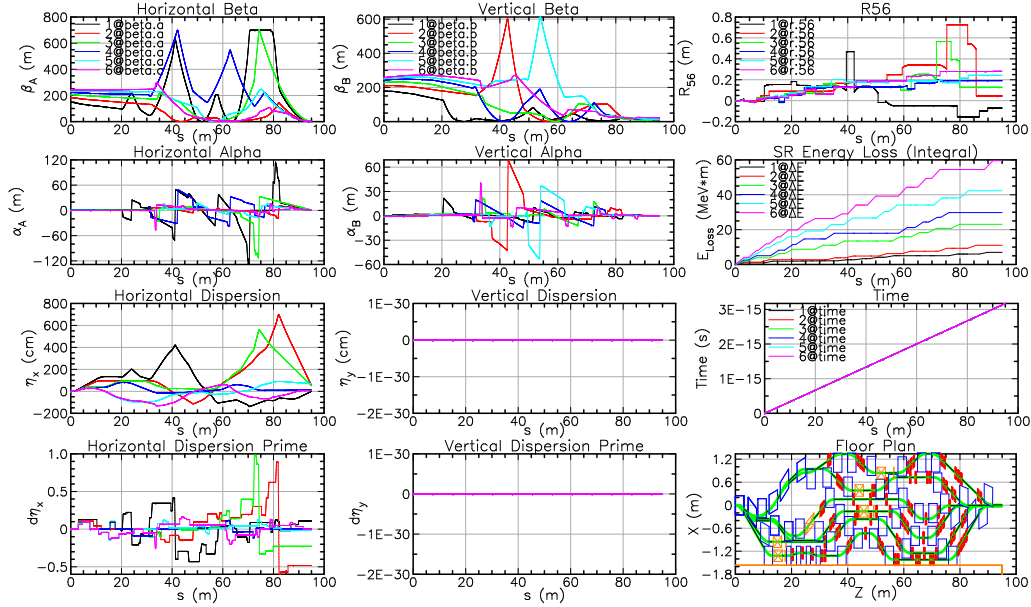


Figure 14: Matching solution from the WFT LINAC input into the BDC FFA match point. In this case, R_{56} and $\beta_{x,y}$ is always matched perfectly, $\alpha_{x,y}$ usually matched very well or perfectly, and η_a and η'_a are matched adequately.

B. Aperture Analysis and Beam Envelope

A key consideration for the viability of the optics solutions presented in this document is whether the resulting beam envelope remains within a reasonable physical aperture, particularly given the large peak β -functions observed in some cases (exceeding 1000 m). This appendix provides a preliminary analysis to address this concern.

The beam size (σ) is determined by the geometric emittance (ϵ_{geom}) and the β -function (β) according to $\sigma = \sqrt{\beta\epsilon_{\text{geom}}}$. The geometric emittance is related to the normalized emittance (ϵ_n) and the relativistic factor (γ_r) by $\epsilon_{\text{geom}} = \epsilon_n/\gamma_r$.

For this analysis, we adopt the projected normalized emittance for the FFA@CEBAF upgrade, $\epsilon_n = 80 \text{ mm} \cdot \text{mrad}$ [4]. We then examine the maximum β -function (β_{max}) encountered for each of the six passes across all matching solutions presented. The required beam-stay-clear (BSC) is calculated based on the standard CEBAF operational requirement of a 10σ envelope.

Table 18 summarizes the results. The worst-case beam envelope occurs

at the location of the maximum value of β_{\max}/γ_r .

Table 18: Calculation of the 10σ beam-stay-clear (BSC) envelope for each pass, using the projected FFA@CEBAF normalized emittance and the maximum β -function found in any solutions presented in this work.

Energy (GeV)	$\approx \gamma_r$	β_{\max} (m)	1σ Size (mm)	10σ BSC (mm)
10.55	20 646	1134.2	2.10	21.0
12.95	25 342	710.2	1.50	15.0
14.95	29 256	1309.7	1.89	18.9
17.15	33 562	1075.5	1.60	16.0
19.35	37 867	1459.0	1.76	17.6
21.55	42 172	869.2	1.28	12.8

The analysis indicates that the largest required beam envelope occurs in Pass 1, reaching a 10σ stay-clear radius of approximately 21.0 mm. This maximum occurs in the solution matching the SFT LINAC input to the "Beginning" FFA match point without R_{56} compensation (Table 6 in Appendix A).

A required aperture radius of 21 mm is well within the typical dimensions of accelerator vacuum chambers (e.g., 40 mm to 50 mm diameter). Therefore, this preliminary analysis confirms that even the largest β -function excursions found in the presented optics solutions do not pose an aperture limitation for the beam. Further detailed tracking studies including misalignment and momentum offsets are planned for future work.

C. Declaration of AI Assistance in this Work

During the preparation of this work the authors used AI tools, mostly Google's Gemini, in order to assist with various elements of the preparation of this work. This assistance includes the formatting of tables and text, checking for overall consistency of the paper, and other small, editorial tasks. After using this tool/service, the authors reviewed and edited the content as needed and take full responsibility for the content of the published article.

References

- [1] J. Grames et al. *Positron Beams At Ce⁺BAF*. Sept. 28, 2023. DOI: 10.48550/arXiv.2309.15581. arXiv: 2309.15581 [physics]. URL: <http://arxiv.org/abs/2309.15581> (visited on 11/14/2025). Pre-published.
- [2] Eric Voutier. *The Jefferson Lab Positron Physics Program*. Jan. 30, 2024. DOI: 10.48550/arXiv.2401.16223. arXiv: 2401.16223 [nucl-ex]. URL: <http://arxiv.org/abs/2401.16223> (visited on 11/14/2025). Pre-published.
- [3] E. Nissen et al. “Design Progress for the 22 GeV CEBAF Energy Upgrade”. In: *Proc. North American Particle Accelerator Conference (NAPAC2025)*. North American Particle Accelerator Conference (Aug. 2025), pp. 664–667. ISSN: 2673-7000. DOI: 10.18429/JACoW-NAPAC2025-WEZN01. URL: <https://indico.jacow.org/event/97/contributions/9576>.
- [4] Kirsten Deitrick et al. “CEBAF 22 GeV FFA Energy Upgrade”. In: (Sept. 26, 23). Ed. by Assmann,Ralph et al., 962–964 pages, 0.66 MB. ISSN: 2673-5490. DOI: 10.18429/JACOW-IPAC2023-MOPL182. URL: <https://jacow.org/ipac2023/doi/jacow-ipac2023-mopl182> (visited on 11/14/2025).
- [5] Stephen Brooks and Alex Bogacz. “Permanent Magnets for the CEBAF 24 GeV Upgrade”. In: (2022). Ed. by Frank Zimmermann et al., 4 pages, 0.715 MB. ISSN: 2673-5490. DOI: 10.18429/JACOW-IPAC2022-THPOTK011. URL: <https://jacow.org/ipac2022/doi/JACoW-IPAC2022-THPOTK011.html> (visited on 11/13/2025).
- [6] S.J. Brooks. “Open-Midplane Gradient Permanent Magnet with 1.53 T Peak Field”. In: (Sept. 26, 23). Ed. by Assmann,Ralph et al., 3870–3873 pages, 1.6 MB. ISSN: 2673-5490. DOI: 10.18429/JACOW-IPAC2023-WEPM128. URL: <https://jacow.org/ipac2023/doi/jacow-ipac2023-wepm128> (visited on 11/13/2025).
- [7] Jay Benesch. *Corrector Concept for FFA Arcs, JLAB-TN-22-034*. URL: <https://jlabdoc.jlab.org/docushare/dsweb/Get/Document-259373/22-034.pdf> (visited on 11/17/2025).

- [8] Alexander Coxe. *FFA@CEBAF: Alignment of Corrector Magnets & BPM Readings in the West FFA Arc*, JLAB-TN-23-068. URL: <https://jlabdoc.jlab.org/docushare/dsweb/Get/Document-277958/23-068.pdf>.
- [9] A.M. Coxe et al. “Status of Error Correction Studies in Support of FFA@CEBAF”. In: (Sept. 26, 23). Ed. by Assmann,Ralph et al., 949–951 pages, 2.3 MB. ISSN: 2673-5490. DOI: 10.18429/JACOW-IPAC2023-MOPL177. URL: <https://jacow.org/ipac2023/doi/jacow-ipac2023-mop1177> (visited on 11/13/2025).
- [10] Alexander Coxe et al. “Beam Correction for Multi-Pass Arcs in FFA@CEBAF: Status Update”. In: (July 1, 2024). Ed. by Pilat,Fulvia et al., 1057–1059 pages, 0.44 MB. ISSN: 2673-5490. DOI: 10.18429/JACOW-IPAC2024-TUPC23. URL: <https://jacow.org/ipac2024/doi/jacow-ipac2024-tupc23> (visited on 11/13/2025).
- [11] Alexander Coxe. “Error and Correction Analysis for the FFA@CEBAF Energy Upgrade”. In: *Physics Theses & Dissertations* (Oct. 1, 2024). DOI: 10.25777/q9mc-vk53. URL: https://digitalcommons.odu.edu/physics_etds/212.
- [12] A. Bartnik et al. “CBETA: First Multipass Superconducting Linear Accelerator with Energy Recovery”. In: *Physical Review Letters* 125.4 (July 23, 2020), p. 044803. ISSN: 0031-9007, 1079-7114. DOI: 10.1103/PhysRevLett.125.044803. URL: <https://link.aps.org/doi/10.1103/PhysRevLett.125.044803> (visited on 11/13/2025).
- [13] Jay Benesch. *First Attempt at a Conductively-Cooled Superconducting Septum Magnet for the FFA Upgrade*, JLAB-TN-22-033. URL: <https://jlabdoc.jlab.org/docushare/dsweb/Get/Document-259326/22-033.pdf> (visited on 11/13/2025).
- [14] Jay Benesch. *Second Attempt at a Conductively-Cooled Superconducting Septum Magnet for the FFA Upgrade*, JLAB-TN-22-037. URL: <https://jlabdoc.jlab.org/docushare/dsweb/Get/Document-259879/22-037.pdf> (visited on 11/13/2025).
- [15] Jay Benesch. *Third Attempt at a Conductively-Cooled Superconducting Septum Magnet for the FFA Upgrade*, JLAB-TN-22-052. URL: <https://jlabdoc.jlab.org/docushare/dsweb/Get/Document-262245/22-052.pdf> (visited on 11/13/2025).

- [16] Jay Benesch. *Extended Lambertson for FFA, JLAB-TN-22-041*. URL: <https://jlabdoc.jlab.org/docushare/dsweb/Get/Document-261003/22-041.pdf> (visited on 11/13/2025).
- [17] Jay Benesch. *ZA Modification Concept, JLAB-TN-22-051*. URL: <https://jlabdoc.jlab.org/docushare/dsweb/Get/Document-261885/22-051.pdf> (visited on 11/13/2025).
- [18] Jay Benesch. *Water-Cooled Copper Septum for FFA, JLAB-TN-22-054*. URL: <https://jlabdoc.jlab.org/docushare/dsweb/Get/Document-262317/22-054.pdf> (visited on 11/13/2025).
- [19] Jay Benesch. *A Simple Modification of DC Current Septa to Reduce Current Density by Half*. Sept. 6, 2023. DOI: 10.48550/arXiv.2309.00619. arXiv: 2309.00619 [physics]. URL: <http://arxiv.org/abs/2309.00619> (visited on 11/13/2025). Pre-published.
- [20] Jay Benesch. *Rectangular Common Dipoles for FFA, JLAB-TN-23-041*. URL: <https://jlabdoc.jlab.org/docushare/dsweb/Get/Document-272883/23-041.pdf> (visited on 11/13/2025).
- [21] Jay Benesch. *Conventional Dipole for FFA Splitters, JLAB-TN-23-016*. URL: <https://jlabdoc.jlab.org/docushare/dsweb/Get/Document-271507/23-016.pdf> (visited on 11/13/2025).
- [22] Jay Benesch. *C Magnet to Allow 11 GeV FFA Tests in BSY Dump Line, JLAB-TN-23-017*. URL: <https://jlabdoc.jlab.org/docushare/dsweb/Get/Document-271580/23-017.pdf> (visited on 11/13/2025).
- [23] Ryan Bodenstern. *Horizontal Splitter Design for FFA@CEBAF: Focus on Geometry JLAB-TN-23-069*. URL: <https://jlabdoc.jlab.org/docushare/dsweb/Get/Document-277999/23-069.pdf>.
- [24] D. Sagan. “Bmad: A Relativistic Charged Particle Simulation Library”. In: *Nuclear Instruments and Methods in Physics Research Section A: Accelerators, Spectrometers, Detectors and Associated Equipment* 558.1 (Mar. 2006), pp. 356–359. ISSN: 01689002. DOI: 10.1016/j.nima.2005.11.001. URL: <https://linkinghub.elsevier.com/retrieve/pii/S0168900205020371> (visited on 11/13/2025).
- [25] T Hiatt et al. “Fabrication and Measurement of 12 GeV Prototype Quadrupoles at Thomas Jefferson National Accelerator Facility”. In: *Proc. PAC’09*. Particle Accelerator Conference (), pp. 223–225. URL: <https://jacow.org/PAC2009/papers/M06PFP037.pdf>.

- [26] B.R. Gamage et al. “Resonant Matching Section for CEBAF Energy Upgrade”. In: (July 1, 2024). Ed. by Pilat, Fulvia et al., 3075–3078 pages, 1.1 MB. ISSN: 2673-5490. DOI: 10.18429/JACOW-IPAC2024-THPC37. URL: <https://jacow.org/ipac2024/doi/jacow-ipac2024-thpc37> (visited on 11/13/2025).
- [27] B.R. Gamage et al. “Design Update on the Transition Beamline for the CEBAF Energy Upgrade”. In: *Proc. NAPAC2025* (Sacramento, CA, USA). North American Particle Accelerator Conference 2025. JACoW Publishing, Geneva, Switzerland, Aug. 2025, pp. 418–421. ISBN: 978-3-95450-261-5. DOI: 10.18429/JACoW-NAPAC2025-TUP029. URL: <https://indico.jacow.org/event/97/contributions/10854>.
- [28] R. H. Helm et al. “Evaluation of Synchrotron Radiation Integrals”. In: *IEEE Transactions on Nuclear Science* 20.3 (1973), pp. 900–901. DOI: 10.1109/TNS.1973.4327284.
- [29] John M. Jowett. “Introductory statistical mechanics for electron storage rings”. In: *AIP Conference Proceedings* 153.1 (Feb. 1987), pp. 864–970. ISSN: 0094-243X. DOI: 10.1063/1.36374. eprint: https://pubs.aip.org/aip/acp/article-pdf/153/1/864/11694813/864_1_online.pdf. URL: <https://doi.org/10.1063/1.36374>.
- [30] R. Kazimi. “An Extraction Scheme for Future CEBAF FFA Based Energy Upgrade”. In: *Proc. IPAC’25* (Taipei, Taiwan, June 1–6, 2025). IPAC’25 - 16th International Particle Accelerator Conference 16. JACoW Publishing, Geneva, Switzerland, June 2025, pp. 1407–1410. ISBN: 978-3-95450-248-6. DOI: 10.18429/JACoW-IPAC2025-TUPM114. URL: <https://indico.jacow.org/event/81/contributions/7637>.
- [31] David Sagan. *Tao Simulation Program*. Tao Manual. Oct. 25, 2025. URL: <https://www.classe.cornell.edu/bmad/tao.html> (visited on 10/27/2025).